

*University of Kent
Masters Thesis*

*Low-speed to high-speed hypervelocity
impacts into sand using a prototype
vertical light-gas gun.*

Dylan Doherty

*A thesis submitted in fulfilment of the requirements for the degree of
Master of Science – MSc*

in the

Centre for Astrophysics and Planetary Science School of Physical Sciences

September 2018

Acknowledgements

Thank you to my mother and father for supporting me every day and always looking out for me.

Thank you to my Supervisor Professor Burchell for all the wisdom and guidance you imparted on me.

Thank you to my friends and girlfriend for pushing me to do my best.

And finally, thank you to Mike Cole, the Experiment Officer, who without, I would not have been able to do any of this.

Table of Contents

Acknowledgements.....	2
Abstract.....	4
Chapter 1: Introduction.....	5
1.1 Impact Speeds	5
1.2 Types of Impact	6
1.3 Crater Formation	9
1.4 Summary.....	12
Chapter 2: The Light-gas gun	12
2.1 The History of The Light-gas gun.....	12
2.2 GMI Light-Gas Gun	16
2.3 Kent Light-Gas Gun	25
2.4 Other Guns	30
2.5 Summary.....	35
Chapter 3: Methodology	35
3.1 Sand Target	35
3.2 Setting Up the Gun	43
3.3 How to Measure.....	50
3.4 Error calculations.....	58
3.5 Summary.....	59
Chapter 4: Result Analysis	60
4.1 The Shots	60
4.2 Pi-Scaling.....	67
4.3 Previous Work	69
4.4 Summary.....	81
Chapter 5: Conclusion	82
References.....	84

Abstract

Hypervelocity impacts are a key field of research in the physics community and has been for several decades now. The University of Kent has been developing a new vertical light-gas gun in an effort to open the pathways for more developed research into the field of planetary science. By building this new light-gas gun, avenues open up for research involving targets previously unavailable to the university, such as low and non-existent cohesion targets such as sand and water.

I was one of the first people to run experiments using the prototype gun and was able to fire 5 successful shots into a sand target at speeds below 1 km s^{-1} . Unfortunately, the gun was unable to fire above this speed, the hope is to achieve above 1 km s^{-1} sometime near the end of 2018. I predicted my results using the pi-scaling method and compared the size and shapes of my craters with that of previous data from Melosh's book *Impact Cratering: A Geological Process* (Melosh, 1989). I found my data fit the pattern of Melosh's despite some changes in magnitude.

This work establishes that the gun is ready for use at speeds up to 1 km s^{-1} . The work can be continued when the gun exceeds speeds of 1 km s^{-1} , extending the sand crater data set into the hypervelocity regime.

Chapter 1: Introduction

1.1 Impact Speeds

In our universe, celestial objects move and collide with each other on a frequent basis. The speed of these projectiles is very fast. We can see typical speeds of objects in our solar system in table 1.1, where we compare the speeds of these objects as they orbit the sun.

Planet	Orbital Speeds (km/s)
Mercury	47.4
Venus	35
Earth	29.8
Mars	24.1
Jupiter	13.1
Saturn	9.6
Uranus	6.8
Neptune	5.4

Table 1.1: A table of the orbital speeds of bodies in our solar system (data taken from the Hyperphysics websites on 10/09/2018)

The speeds in Table 1.1 are given by equation 1.1:

$$v = \sqrt{GM/r} \dots (1.1)$$

where v is the speed, G is the Universal gravitational constant, m is the mass of the body and r is the distance from the body to the Sun.

As can be seen from table 1.1, the speed of objects in our solar system tend to be in the degree of km s^{-1} . Match this with the data from table 1.2, which describes the infall speeds of planets in our solar system, and you begin to see the range of velocities planetary scientists have to take into consideration when looking at impact velocities between cosmic objects. The speeds in table 1.2 are set by the mass of each body, hence the high escape velocity of Jupiter. A further complication concern moons which orbit the planets. They will have their own orbit speed around the planet (similar to

table 1.1 for planets orbiting the sun) and might be struck by objects falling towards the planet. But again, these impact speeds will typically be in the region of km s^{-1} .

The escape velocity is equal to the speed of your fall from infinity to the planets surface and is given by equation 1.2:

$$v = \sqrt{2Gm/R} \dots (1.2)$$

where v is the escape velocity, G is the universal gravitational constant, m is the mass of the body, and R is the radius of the body.

Planet	Escape Velocity (km/s)
Mercury	4.3
Venus	10.4
Earth	11.2
Mars	5
Jupiter	59.5
Saturn	35.5
Uranus	21.3
Neptune	23.5

Table 1.2: Planets in our solar system with corresponding escape velocities (data taken from the Hyperphysics website on 10/09/2018).

As you can see when dealing with potential impact velocities, the speeds are again in the km s^{-1} range. However, on Earth it is difficult to recreate impact speeds in this degree. This is where the need for the light-gas gun came from. The light-gas gun allows scientists to accelerate particles to speeds in the km s^{-1} through a process described later in this paper.

1.2 Types of Impact

To study impacts at these speeds we thus need special facilities with targets and projectiles. These targets and projectiles need to reflect the environments that happen in our solar system, which can mean any combination of materials such as: sand (see Schmidt and Housen, 1987), rock (see Burchell and Whitehorn, 2003, Morris and

Burchell, 2017 and Shrine et al., 2017), ice (see Shrine et al., 2002, Grey and Burchell, 2003, Fendyke et al., 2013 and McDermott, 2016), steel or any other metals (see Burchell and Mackay, 1998, Burchell et al, 1999, and Davison et al., 2011). Some experiments also look into the possible effects hypervelocity impacts can have on satellites, making sure they are strong enough to withstand objects impacting them at these speeds (e.g see Leliwa-Kopystynski, 2016 and Kearsley, 2017). For some of these materials extra steps need to be taken to ensure a successful experiment. As can be seen from the recent dating of a lot of these papers, this field is massively popular at the moment and there is still much work to be undertaken by scientists to begin understanding the nature of hypervelocity impacts and their consequences. Many papers based on the study of hypervelocity impacts use many different materials and targets:

- Characterising primary fragments in debris cloud formed by hypervelocity impact of spherical stainless-steel projectile on thin steel plate (Verma et al., 2018).
- Hypervelocity Impact experiments on metallic body (Libourel et al., 2018)
- Investigation of hole formation by steel spheres impacting on thin plates at hypervelocity (Dhote et al., 2018)
- Hypervelocity impact tests on metal mesh materials (Higashide et al., 2005)
- Hypervelocity impact experiments on solid CO₂ targets (Burchell et al., 1998)
- Experimental damage evaluation of honeycomb sandwich structures with Al/B4C FGM face plates under high velocity impact loads (Arslan and Gunes, 2018).

Hypervelocity impacts are impacts generally in the range above 2 km s⁻¹. To more accurately describe them would be to explain that when the impact occurs the energy of the impact is delivered faster than it can be dissipated, causing extreme transient densities and temperatures. Therefore, the definition of a hypervelocity impact relies not just on the speed of the impact, but also on the materials involved. These types of impacts occur naturally throughout our solar system, where bodies travelling at very high km s⁻¹ encounter one another, collide with each other and, dependant on the

bodies involved can combine to form a new bigger body or possibly vaporise or damage each other.

In this thesis I'd like to explore the craters formed in sand from a projectile over a range of low-speed to high-speed, tracking the changes in the crater characteristics formed and comparing it with that found from a pi-scaling prediction model based on past results. Parallel to this research, was the development of the vertical light-gas gun at the University of Kent campus in Canterbury. As part of my work during this thesis I sometimes assisted Mike Cole, the University Experimental Officer in the Impact Laboratory, with development of the gun in transitioning it from only been able to shoot at low-speeds ($< 1 \text{ km s}^{-1}$) to a high-speed ($\geq 1\text{km s}^{-1}$) gun. This paper will be the first experimental programme undertaken parallel with the development of the light-gas gun.

I chose to use a sand target for several reasons. Firstly, I wanted a cohesionless target, but one in which craters could survive and not collapse under the effects of gravity like water would. I wanted it to be able to flow, so I could capture a crater at the moment of impact, and it would be easy to measure and collect data from. Secondly, I wanted to simulate in position a regolith, a loose fine-grained material sound covering many (rocky) planetary surfaces. However, I am aware that the sand particle to projectile particle size ratio, is not necessarily accurate for normal regolith on different solar system bodies, and that the experimental data will differ from real life data due to that. Also, my experiments will occur with small projectiles so will be in a regime where crater growth is dominated by strength, and not by gravity. For larger impacts on real bodies (i.e impactors $>$ a few 1000 m) gravity effect will dominate.

1.3 Crater Formation



Figure 1.1: Barringer Meteor Crater (Arizona) photo taken by D. J. Roddy. (<https://ai2-s2-public.s3.amazonaws.com/figures/2017-08-08/443b08b1f64c775bc063fbecbf1ca665757c2cbc/2-Figure1.1-1.png>)

In figure 1.1 we can see a classic example of an impact crater. Barringer Meteor Crater in Arizona is approximately 1.186 km in diameter and 170 m deep. It has a 45 m rise and is over 50,000 years old (<https://www.barringercrater.com/the-crater/#history-banner>, Kenkemann, 2018). A crater has several identifying features, including the raised edges, a small rise in the middle (depending on the size of the crater, with a simple bowl shape for areas up to a few km diameter, and a central peak appearing in larger craters depending on the local gravity) and the complex deformation effects they leave behind.

There are several stages to a crater's development, starting with the contact/compression stage and ending with the final crater. Bevan French in his book *Traces of Catastrophe* (1998) has a very good series of images that compares the different stages of a crater's birth, as shown in figure 1.2.

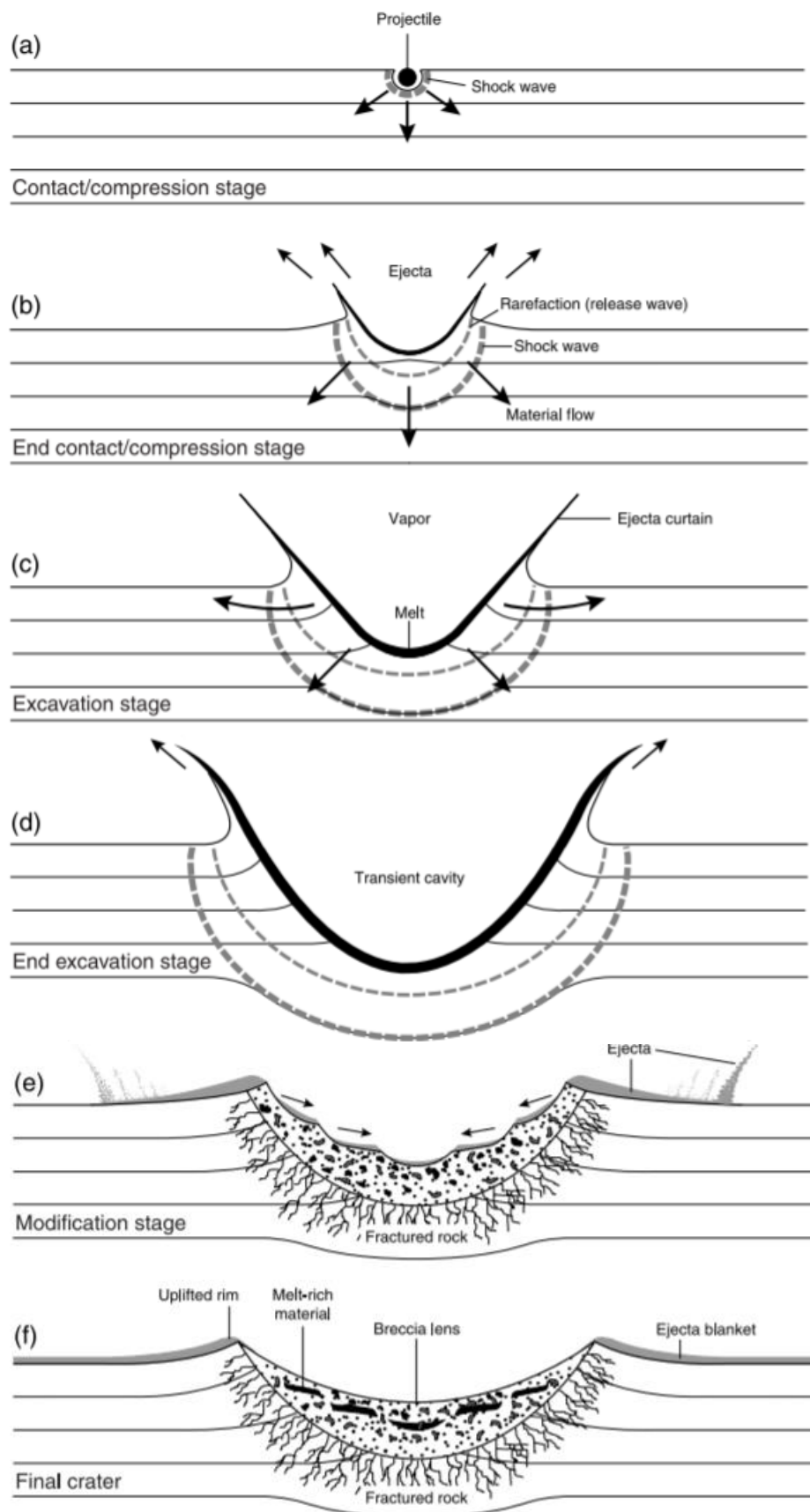


Figure 1.2: The 'birth' of a crater (French, page 23, 1998).

As can be seen in Figure 1.2, the initial contact of the projectile begins to send shockwaves into the target. Next rarefaction begins around the surface area and ejecta begins to fly away from the impact, shock waves continue, and material begins to flow deeper into the target as well, this is known as the end contact/compression phase. Next is the excavation phase, the absolute bottom of the crater begins to melt, and vapours are released, a curtain of ejecta forms and the crater begins to move outwards as the downwards momentum begins to slow. The final excavation phase is next where you see a transient crater with ejecta yet to be settled. Once the ejecta lands, it is called the modification phase. This is where the material begins to collapse in on itself under gravity and the compressed rock in the base of the crater can begin to fracture. The final stage is the emergence of the final crater - you are left with an ejecta blanket all around the crater, an uplifted rim, along with melt-rich material and breccia lens. In figure 1.3 we can see a diagram explaining where all the material from before an impact goes during an impact.

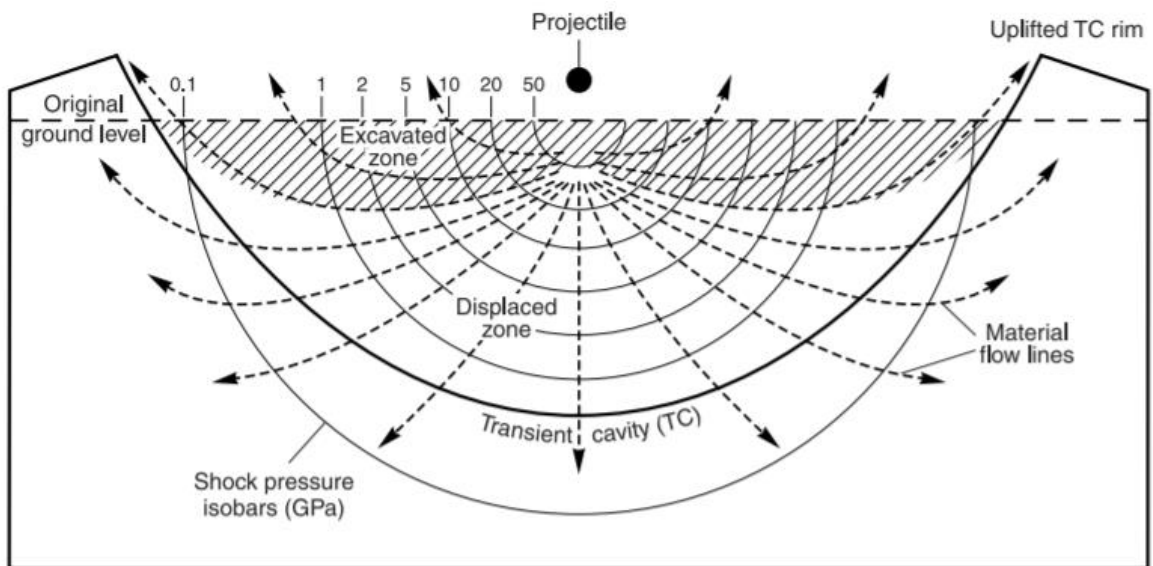


Figure 1.3: An in-depth analysis of the transient crater formation. (See French, pp. 22, Fig 3.4, 1998).

1.4 Summary

In the rest of this these I will describe the nature of the light-gas gun in general (see chapter 2), my experimental method for impacts in sand (see chapter 3), my results and analysis (see chapter 4) and finally my conclusions (see chapter 5).

Chapter 2: The Light-gas gun

2.1 The History of The Light-gas gun

The two-stage light-gas gun emerged into the public eye in the year 1957 with a paper from W. D. Crozier and W. Hume called ‘High-Velocity Light-gas gun’ (Crozier and Hume, 1957). As this was a time of great tension between the two superpowers (the US and USSR), the light-gas gun had not been made public knowledge before. This was due mainly to the light-gas gun potential use in warfare. However, today they are widely used in impact research for material physics, planetary science, space craft design and other relevant fields.

Crozier and Hume’s paper is a good starting point for the history of the light-gas gun, as it highlights early problems encountered by scientists and details the early capabilities. Before the use of light gases such as hydrogen and helium, powder propellants were used to accelerate the gases in guns, and this was proving to be a principle factor in limiting the potential muzzle velocity attainable. One attempt that was made to overcome this was by increasing the powder charge and density of the loading and decreasing the projectile mass (Crozier and Hume, 1957). This would result in a large pressure gradient in the column of powder gas behind the projectile. However, the ratio of base to breech pressure became too small and due to the limits on the breech pressure, the force available for accelerating the actual projectile becomes small also, one would begin to receive diminishing returns as the muzzle velocity was pushed beyond 1500 m s^{-1} (Crozier and Hume, 1957). This was proved by Langweiler (1938), who showed that with an enormous breech pressure of 12300 Bar, the muzzle velocity approached approximately 2800 m s^{-1} as the projectile mass

approached zero. Therefore, any projectile with a useful weight would only be likely to reach a maximum speed in the vicinity of 2400-2750 m s⁻¹.

In 1946 Corner proposed that a new range of muzzle velocities may be attained if the column of conventional powder gas (with an effective molecular weight of 20 to 25) was replaced with a gas of low molecular weight (Corner, 1946). In 1947 a gun that used this method was produced and performed as predicted, spawning the creation of several more guns of this type in the years that followed (Crozier and Hume, 1957). Crozier and Hume explain that they felt the guns were excellent for accelerating projectiles to very high velocities for “the study of exterior and terminal ballistics but are also excellent for studying the properties of gas at high pressures and temperatures under nearly adiabatic conditions”. To achieve these conditions necessary for such a study, the gun has to be made to be a very tight fit at all joints and junctures, so as to prevent as much leakage as possible during the projectile’s travel down the barrel.

We can see their gun schematic in figure 2.1 below. Crozier and Hume break down the mechanical functions of the gun in their paper. First the bore of the pump tube is filled with helium or hydrogen to a fixed pressure through an inlet, and a valve is then closed in the inlet line. Next the charge is fired, and the piston moves down the bore, compressing the light gas. The inertia of the piston means the maximum light gas pressure behind the piston is greater than the pressure behind the powder. What happens next then depends on the shape of the projectile. If it is a slug it shears out of the flange, and if it is a sphere it is forced through the supporting ring. In this case an expendable energy absorber is installed to prevent damage to the rest of the gun.

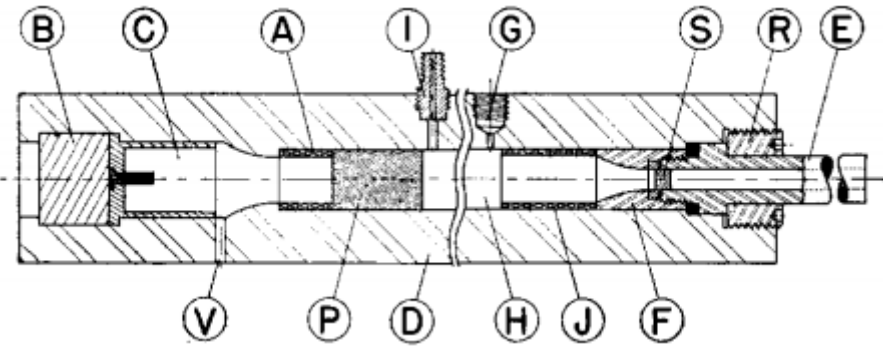


Figure 2.1: Schematic drawing of the gun from Crozier and Humes 1957 paper (figure 1) where:

- A. Energy Absorber 1, B. Charge, C. Conventional Powder Chamber, D. Cylinder, E. Gun Barrel, F. Throat Piece, G. One placement for Pressure gauges, H. Bore, I. Inlet, J. Energy Absorber 2, P. Piston, R. Screw Ring, S. Cylindrical Slug, V. Vent.

Preliminary calculations were made on a gun by Crozier and Hume (1957), to fire a steel cylinder 7 mm in diameter, weighing 2 g. The authors assumed simple gas laws for hydrogen, adiabatic conditions, the Kent (Kent, 1936) structure for the light gas column, and a maximum hydrogen pressure of ~6900 Bar. For a limiting case where the compression of the hydrogen pressure was started from a standard condition a muzzle velocity of 2100 m s^{-1} was calculated. For a case where it was ~690 Bar with ambient temperatures, the muzzle velocity was calculated to be 3050 m s^{-1} .

For a practical design, several considerations had to be known or set: (1) The equation of state for hydrogen, and its initial pressure, temperature, and the volume; (2) the diameter, mass, and distance of travel of the piston; (3) the length of the column of the powder chamber and the mass and burning characteristics of the powder charge; (4) the pressure at which the projectile is released; and (5) the mass, calibre, and the distance travelled by the projectile (Crozier and Hume, 1957). Usually there would also be considerations for the loss of heat to the walls and frictional forces on the projectile and piston, but these were neglected, although they would be fully integrated in a complete treatment. Adiabatic conditions were assumed and using Bridgman's (Bridgman, 1949) isothermal data, a hydrogen adiabatic p-v curve was derived. For a

significant end hydrogen volume post compression, the initial pressure had to be in the order of 100 Bar.

Crozier and Hume found that, as they had predicted, the maximum hydrogen pressure and the muzzle velocity increased as the piston mass and velocity were increased. However, as the piston mass varied the muzzle velocity varied very slowly, thus keeping the piston energy constant. As tests of the gun were made, more refined calculations were also made, and in five selected cases the calculated and observed muzzle velocities only differed by less than 8% (Crozier and Hume, 1957). Mainly hydrogen was used, however in 10 cases it was replaced with helium in an effort to reduce muzzle flash allowing for photographic studies to be made. An early problem was found with oil in the barrel causing large drag and erosion of the projectile, this was easily fixed by making sure to use a dry barrel. There was slight gas erosion, but this was minimal due to the relatively low temperatures the hydrogen reaches (1100 K) as opposed to the previously used conventional propellant temperatures (2000-3000 K). Crozier and Hume concluded that the first model of LIGHT-GAS GUN had fully demonstrated that a light gas propelling column could deliver muzzle velocities considerably higher than what was being previously delivered by columns of conventional powder gas and a table of their results can be seen in table 2.1.

Round	Gas	Projectile Mass (g)	Caliber (in.)	Barrel length (in.)	Initial light gas Pressure (lb/in. ²)	Temperature (°C)	Maximum pressures Powder gas (lb/in. ²)	Light gas (lb/in. ²)	Muzzle velocity (ft/sec)
13	H ₂	2.46 ^a	0.32	39	1225	16	14 500	132 000 (est.)	11 000
29	H ₂	3.51	0.37	39	1140	29	17 200	146 000	11 280
37	H ₂	3.51	0.37	39	1255	16	15 000 ^b	110 000	11 070
48	H ₂	3.87	0.39	54	1250	5	15 000	100 000	11 970
60	H ₂	3.87	0.39	54	1250	17	17 200	121 000	12 330
63	H ₂	4.42	0.41	51	1235	11	15 400	103 000	11 180
70	He	4.47	0.41	51	1240	17	19 000	115 000	10 700
74	He	3.50 ^a	0.37	39	1120	10 200
81	H ₂	4.47	0.41	51	1210	21	14 000	115 000 ^b	12 230

^a Cylindrical slugs; other rounds used spherical projectiles.

^b Pressure not measured, but obtained from comparable rounds.

Table 2.1: Results of the light-gas gun from Crozier and Hume, 1957.

2.2 GMI Light-Gas Gun

To get an idea of LIGHT-GAS GUN development and the problems that scientists faced over time, consider Stilp's 1987 paper 'Review of Modern Hypervelocity Impact Facilities' (Stilp, 1987). Thirty years after Crozier and Hume's paper, Stilp reviewed the Hypervelocity impact ranges of the German Ernst-Mach-Institut (EMI) also known as the Fraunhofer Institute for High-Speed Dynamics. Prior to the year 1965, the research in this area was mainly restricted to the US and Soviet Union, mostly being focused on requirements for their space and weapons program. At the time this later paper was written, other nations had begun to make efforts to catch up with the new developments and make their own unique contributions. The EMI was equipped with 7 closed indoor ranges; 3 of which had two-stage LIGHT-GAS GUNS, with launch tube calibres varying from between 4.5 and 40 mm; these are the focus of the paper. All 3 of the ranges were indoors and closed off with similar basic construction. They are made up of 4 main components: the launcher system, an interface with the blast tank, a sabot stripper and velocity measurement system, and the impact tank. Many of these parts are interchangeable giving them a high measure of flexibility (Stilp, 1987).

The first range, referred to as Range I, has been in operation since 1968 and is equipped with the largest LIGHT-GAS GUN out of the three ranges; an image of which can be seen in figure 2.2. The launcher is a hybrid-type launcher and stores energy differently. For slower shots ranging up to 500 m s^{-1} the launch tube is connected by hydraulic clamp to a high-pressure compressed gas reservoir (Stilp, 1987). Accurate velocity measurements are attained, and costs are low. When velocities up to about 2.5 km s^{-1} are required, solid propellant is used; for this application the smooth-bore launch-tube is connected by the hydraulic clamp to a powder chamber. To get higher impact velocities with low acceleration forces, compressed and heated helium is used in the two-stage light-gas gun.

In Range I, smooth-bore launch tubes with calibres from 10 to 40 mm are used. The pump tube for the first stage of the LIGHT-GAS GUN has a 65 mm calibre with a length of 6.5 m. There is also a high-pressure section of two high quality steel parts with a transition angle of 5 degrees. Stilp (Stilp, 1987) goes into detail about the (at the time)

'new' techniques for high-pressure sealing (delta-ring seals) that were used to make the important connections between the launch tubes, diaphragm, and the high-pressure sections. CrNi-Steel was used to make the powder chamber, pump tube, high pressure sections and launch tube. All of the parts are mounted on a solid steel foundation. The pump tube and high-pressure section are on rollers, which allows them to be moved axially to insert the projectile or connect the pressure reservoir or powder chamber to the launch tube for ordnance allowing for simpler movements and flexible applications. The piston is made from polyethylene with lead inserts that increase the mass to 5 kg (Stilp, 1987). The launch tube is connected to the blast tank by an axial compensator. The blast tank is 3 m long and 1.5 m in diameter and has 20 mm thick steel walls. It also has four windows, each 200 mm in diameter for two shadowgraph stations used for measuring speed, and an access door for easy installation of heavy sabot catchers.

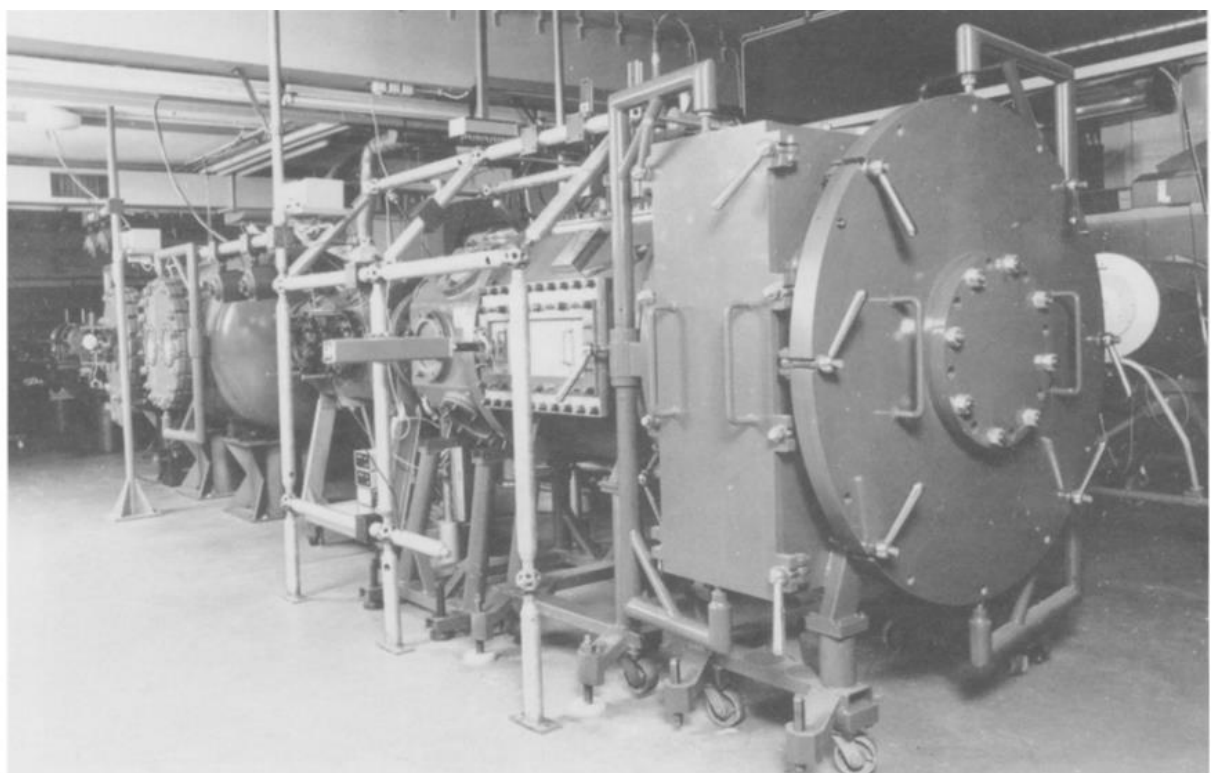
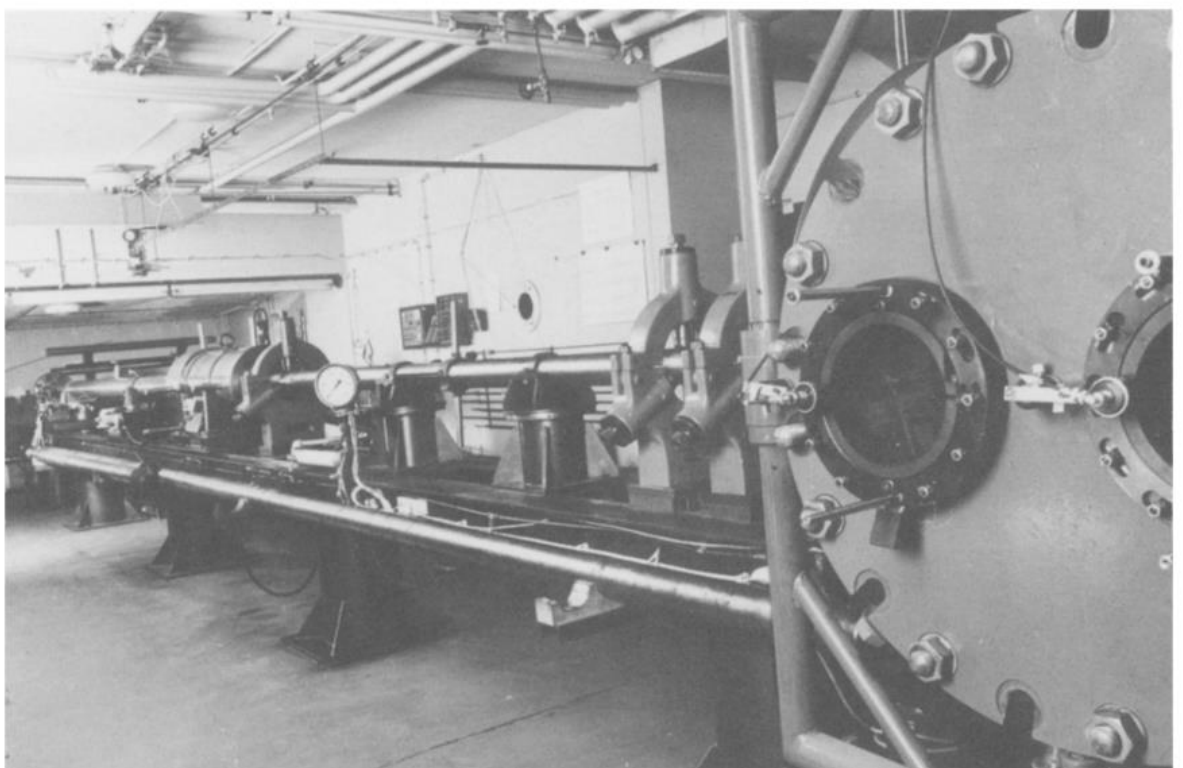


Figure 2.2: Photographs of the LIGHT-GAS GUN, Range 1, at the EMI, Germany. (Stilp, 1987)

There is another velocity measurement station in the entrance of the impact tank, where, similar to the blast tank, there are two shadowgraph systems each with their own trigger delay electronic device. There is a 5 m W helium-neon laser aligned with the trajectory of the projectile and a photodiode on the opposite position of the station. When the projectile interrupts the beam, an electrical signal from the diode triggers a spark point light source, which is the focus of a spherical mirror (Stilp, 1987). This light then enters the two windows of the station where a lens with the diameter of the window collects the parallel light into a camera. The two-point light sources also start and stop an electronic counter; with this information along with the distance of the projectile you can calculate the velocity of the projected to an accuracy of 0.5% (Stilp, 1987). Further to this, the shadowgraph pictures give information about sabot separation and the orientation of the projectile. A diagrammatical breakdown of this method is seen in figure 2.3.

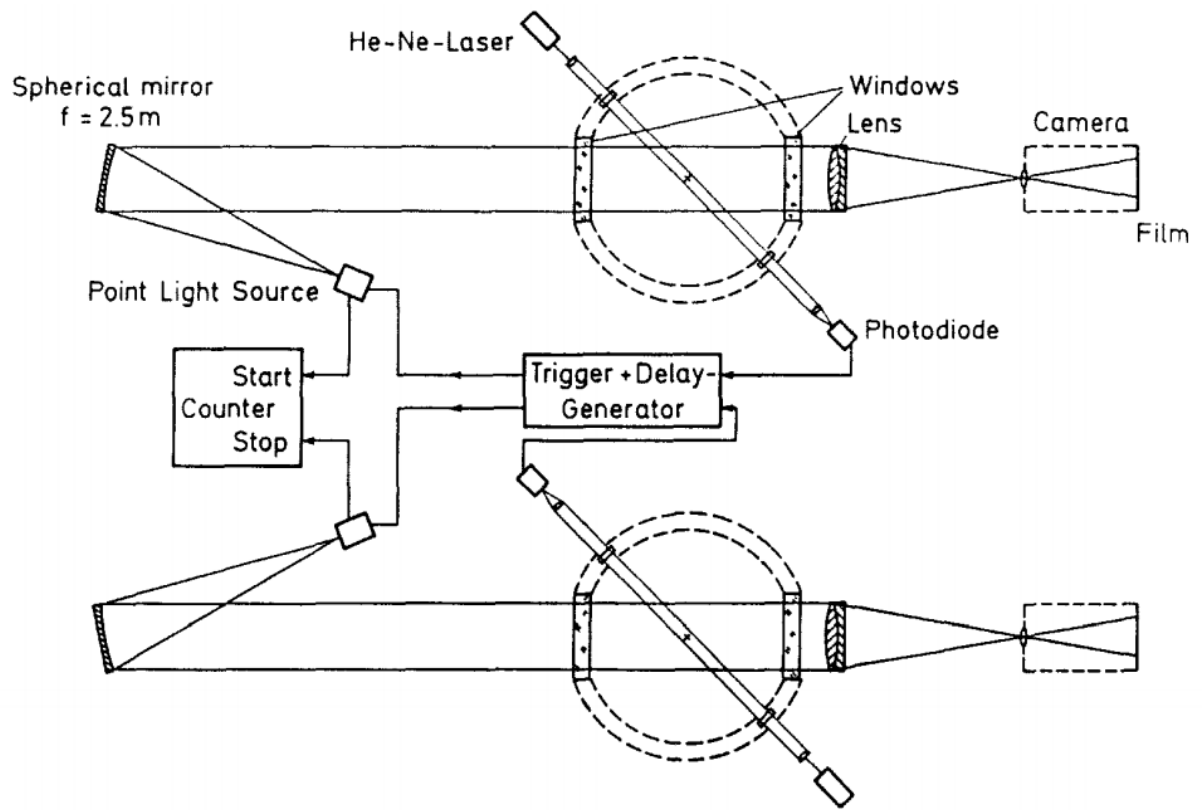


Figure 2.3: Range 1 velocity measurement system at the EMI, Germany. (Stilp, 1987)

The final element in the range is the impact tank, which is made up of three separate modules. Present in the impact tank is the sabot catcher, target holders, X-ray film holders, fiducial line holders, and catchers to stop the fragments and debris generated by the impacts (Stilp, 1987). The modules are 3 m long and 1 m in diameter, with 15 mm thick steel walls. Different windows on all sides of the chamber allow for observation of the process from different angles and positions for flash X-rays or other high-speed photographic instruments. A unique quality of this chamber is that the dimensions allow the installation of a special ballistic pendulum, which is able to measure the momentum transferred to the target and the momentum of the fragments formed in front of and behind the target (Stilp, 1987). In combination with a flash X-ray arrangement, this pendulum can allow the measurement of energy and momentum balances for different impact situations. An exhaust and vacuum pumping system is connected to the range which reduces the internal pressure, which has two advantages: firstly, this reduces the muzzle blast effects, and secondly it influences the aerodynamic forces acting on the discarded sabot.

Finally, Stilp (1987) details the main instrumentation used in Range I:

- Four stereo 180 kV X-rays channels.
- One stereo 300 kV X-ray channel.
- One 600 kV X-ray channel.
- TRW-image converter camera for streak and framing.
- Special ballistic pendulum.
- Multichannel target temperature and pressure measurement system with transient recorders.

Stilp (1987) goes on to talk about Range II next. Designed and built in 1982, the range was developed due to the need for a new gun that could reach the highest available velocities. As well as needing to be able to perform to a high standard, the gun also needed to be very flexible for a large spread of applications, and as low-cost operationally as could be reasonable. This light-gas gun is broken down into several components; the pump tube has a changeable diameter that can range from either 30, 34 or 40 mm, and the length is 200 cm. The transient angle of the high-pressure

section is 5 degrees and the propellant gas used is hydrogen which can range from a pressure of anywhere between 1 and 15 Bar. The piston is changeable and can weigh between 100 and 300 g and is made of polyethylene. The diaphragm is made of a high ductile stainless steel with a four-petal opening configuration. Delta-steel rings were also used for this gun along with a hydraulic clamp for security. Finally, the powder used could weigh anywhere up to a maximum of 150g. Speeds which are reached in different experiments are detailed in table 2.2 below.

Projectile Type	Diameter [mm]	Mass [mg]	Total Mass Sabot + Proj. [mg]	Velocity [km/s]
Al-Sphere	2	12	225	9.35
Al-Sphere	1.5	10	220	9.6
Al-Sphere	4	95	375	8.5
Glass-Sphere	1.5	5	220	9.0
Glass-Sphere	4	90	370	8.5
Ti-Sphere	4	180	680	6.6
Hard-Metal-Sphere	4	500	1200	5.5
Steel-Cylinder	3	130	600	6.6

Table 2.2: Data results taken from Range II of the EMI, Germany (Stilp, 1987) using an 8.5 mm launch tube calibre.

Similar to Range I, the range consists of a velocity measurement station, a blast tank and an impact tank. However, in this range, the blast tank and impact chamber are on separate vacuum pump systems allowing for two different pressure levels in both systems. The LIGHT-GAS GUN and the blast tank are in completely different rooms, a sketch of the set-up can be seen in figure 2.4 and a photograph of the range can be seen in figure 2.5. The velocity measurement system is different from Range I. In this range an in-flight, interrupted laser beam is combined with a photographic system to give accurate speed measurements. A Beckman and Whitley spark gap light source is used to backlight the projectile whilst a Beckman and Whitley image converter cameras take 5 -10 ns exposures. The target chamber is made of steel approximately 80 cm in diameter and 75 cm deep. Four 150 kV flash X-ray channels are arranged perpendicular to the flight path of the projectile, usually horizontally but can be switched to a vertical plane if need be. The x-ray film cassettes are inside the blast tank

as well but are protected by Pertinax shields. Figure 2.6 shows the velocity measurement system in diagrammatic form.

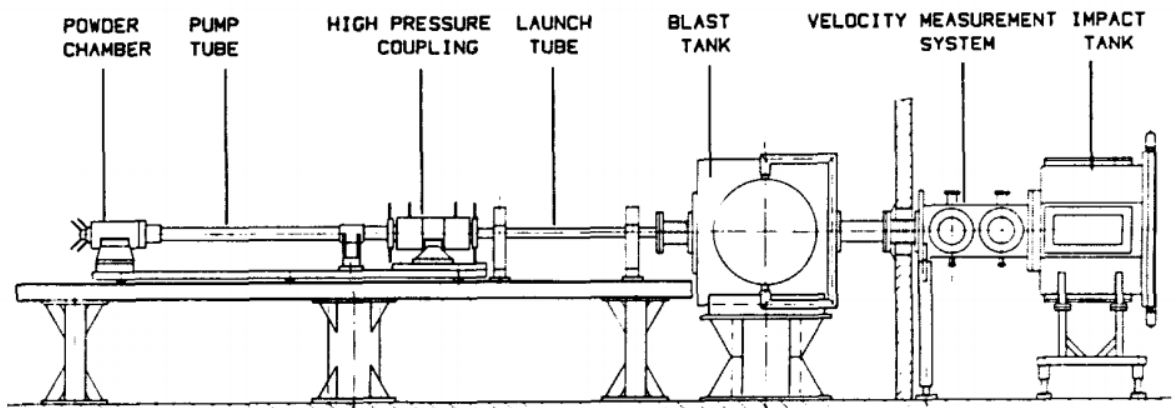


Figure 2.4: Sketch of the Range II set-up at the EMI in Germany (Stilp, 1987)

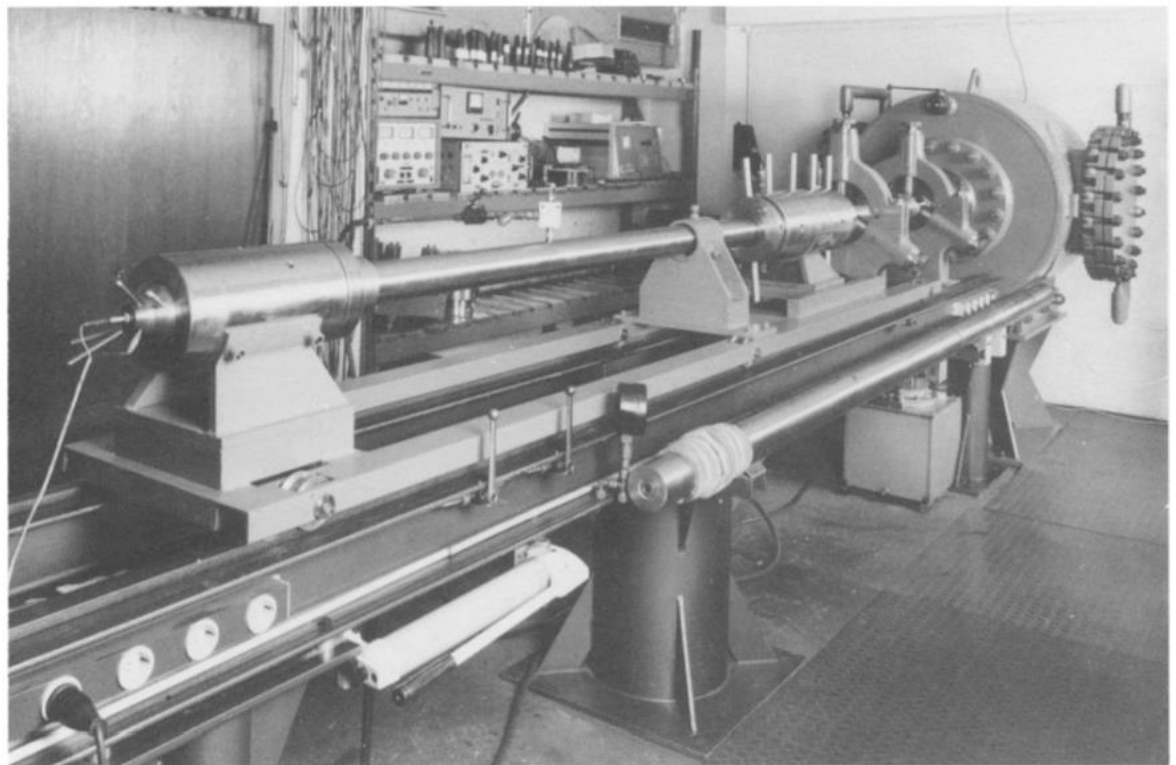


Figure 2.5: Photograph of Range II at the EMI in Germany, with the blast tank (Stilp, 1987).

For firing objects, low-density projectiles such as glass or aluminium use two or four-piece polycarbonate sabots, which are cut with a razorblade. The cutting-device has a mechanism so as to control how deep the cut will be. For heavier, more dense projectiles such as copper, steel or tungsten a two-piece aluminium cup is fitted into the polycarbonate sabot, where the cup has a hole for the projectile. With this there is prevention from punching the heavy density projectile through the polycarbonate sabot when it is accelerated.

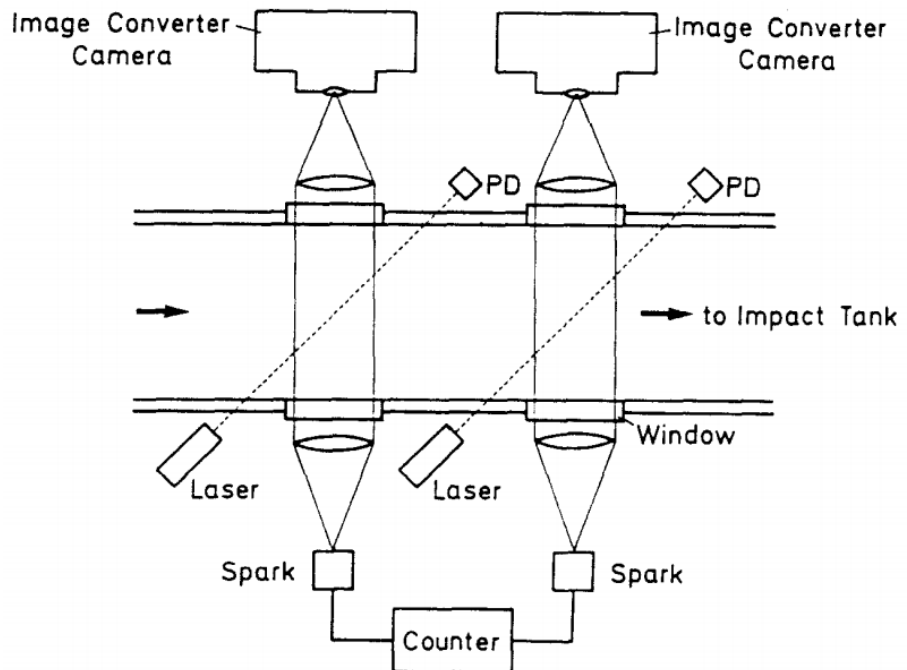


Figure 2.6: Sketch of velocity measurement system on Range II at the EMI in Germany (Stilp, 1987).

Range III is the final range detailed by Stilp (1987). This range is the smallest range of the three. It is mainly used for low-cost hypervelocity experiments, especially for micrometeorite and space debris impact simulations. Only one technician is needed, and the launcher is a two-stage, table-sized LIGHT-GAS GUN with an overall length of 1.5 m. The calibre of the pump tube is 15 mm and a semi-automatic honing device was developed for the production of pump tubes. This device allows for a high-quality bore finish and means there is a significant reduction in launcher problems. Similar to the

two previous ranges, Range III also consist of: a blast tank, a velocity measurement station, sabot catcher box and an impact chamber. The impact chamber is a stainless-steel tank with four windows on each side and a door at the rear side to permit easy installation of the target and precise alignment. A high vacuum pumping system can reduce the pressure in the impact tank to levels in the range of 10^{-6} torr. Unfortunately, Stilp (1987) neglects to mention, the size of projectiles Range III can fire, or the speeds they can reach.

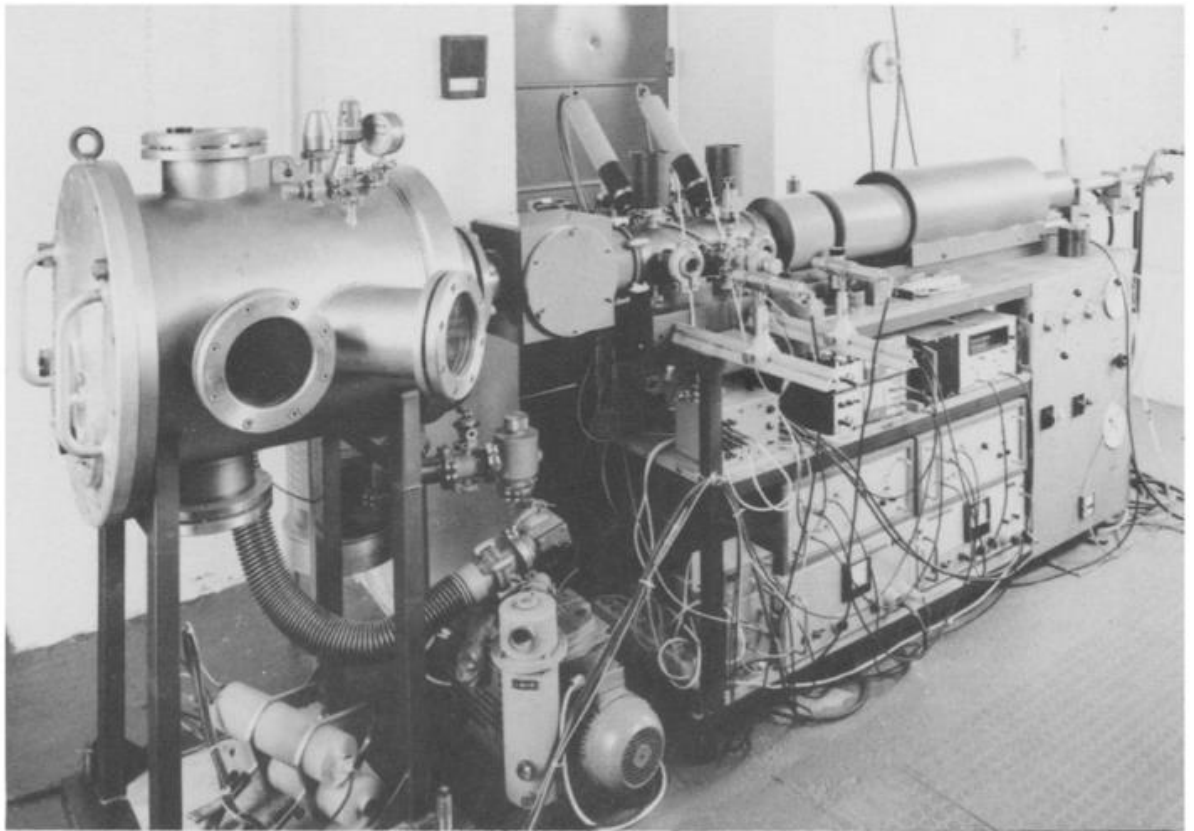


Figure 2.7: Range III from the EMI, Germany including the steel blast tank, LIGHT-GAS GUN and velocity measurement system.

Range III has a unique velocity measurement station specially developed for the detection of small particles. The trigger system, developed specifically for this station, consists of two-bright light sources focused on the trajectory of the projectile. When the projectile passes these light spots, light reflects off the projectile surface and is reflected into photomultiplier tubes. This creates an electric signal to trigger two

sparks with a duration of about 20 ns which are the light sources for the two shadowgraph stations (Stilp, 1987)

The guns are involved in the development of several research programs. This includes activities in thermal ballistics, and several areas of impact physics including: hypervelocity impact research, meteorite bumper design, studies into the damage potential of simulated micrometeorite and space debris particles, and finally the improvement of the range's capabilities and the development of its instrumentation. Stilp concludes that these guns cover a surprisingly large range of instruments applicable to the basic research areas, and the intention was to develop and improve the facility, moving the areas of research forward into the future.

2.3 Kent Light-Gas Gun

The University of Kent has a two-stage light-gas gun, similar in some respects to range III in Fraunhofer. This is described in Burchell (1999). This paper also describes an electronic dual accelerator; but here we only discuss the light-gas gun. At the time, two-stage light-gas gun would fire millimetre-sized particles at $1\text{-}5.7 \text{ km s}^{-1}$. A key research area for the light-gas gun was the investigation of the volume of craters in metal targets for impacts of 1 mm diameter stainless steel spheres on aluminium at velocities in the range of $2\text{-}5 \text{ km s}^{-1}$. Burchell et al. go on to talk about the labelling of hypervelocity impacts. It is common to label any impact above $2\text{-}3 \text{ km s}^{-1}$ as a hypervelocity impact. However, it would be more accurate to describe them as any impact where the energy of the impact is delivered faster than it can be dissipated, which causes extreme transient densities and temperatures at the impact site. As such, there is no hard speed threshold, rather it depends on the materials involved. Space scientists have had a very persistent interest in studying hypervelocity impacts, mainly to understand planetary cratering records and to learn more about the flux and nature of the dust in the solar system. In the solar system, impacts are often in excess of a few km s^{-1} , so are routinely considered as hypervelocity impacts.

The basic operation of the Kent gun is broken down into several steps (Burchell et al., 1999). The initial acceleration of the piston is provided by burning a powder charge, this piston then compresses the low molecular gas. Once the gas reaches a certain pressure the diaphragm (sealing the far end of the pump tube) will rupture releasing the gas and accelerating the projectile down the launch tube. For a given energy, the final velocity of the projectile can be determined by the inverse of the square root of the mean relative molecular mass; therefore, the lighter the second-stage gas the greater the velocity.



Figure 2.8: The horizontal light-gas gun at the University of Kent (circa 2009) (Hibbert et al. 2017)

The Kent gun uses a standard shot-gun cartridge (20 mm diameter) and contains a primer (type CCI 209M) and is typically filled with 10 g of powder (type Alliant reloader 19 or 22) (Burchell et al., 1999). The piston is 8 cm long and has a mass of 12 g. Positioned along the length of the piston at 6 and 6.5 cm are circular grooves, where the 'O' rings sit. These 'O' rings ensure a gas-tight seal in the pump tube from the piston. An example shot scenario given by Burchell is for a speed of 5 km s^{-1} . The pump

tube will be filled with hydrogen gas to a pressure of around 40 Bar. The pump tube is connected via a breech tube to the launch tube, where an aluminium bursting disk separates the two tubes. For a shot the launch tube and all the chambers downstream of the sabot have their pressures reduced to around 0.1 m Bar before firing. When firing the gun, a firing pin is inserted so as to make contact with the base of the cartridge. A pendulum is then placed at 50 degrees from the vertical. When released electronically the operator does so from outside the room, the pendulum swings down and impacts the firing pin, triggering the cartridge. There is more than one type of sabot available, it can either be a single solid piece of nylon weighing about 78 mg or it can be a split sabot that is cut into two or four parts.

The split sabot works by locking together serrated edges when the sabot is confined in the launch tube, which during acceleration stops the relative motion of the sabot. As the sabot then travels down the bore of the gun, it obtains a spin from the rifling in the launch tube, and as it exits the tube and travels through the blast tank, the individual components of the sabot have gained some rotational components to their velocity. Once out of the narrow bore tube and no longer constrained, they travel slightly off the main gun axis at an angle of around 6 degrees (Burchell et al., 1999); this then leaves the projectile on the main flight path. A stop plate is located at the end of the blast tank, where the off-axis sabot shards will collide, and the on-axis projectile will pass through the central 1 cm hole. This stop plate also has an impact sensor made of polyvinylidene difluoride (PVDF), which when flexed by the shock waves transmitted by the sabot, produces an electrical signal, which can then be monitored by an oscilloscope.

After the stop plate, the projectile finally leaves the blast tank which has a width of 0.3 m and a length of 0.9 m. The projectile then passes through two laser-light curtains. The lasers are 3 mW, CW laser diodes, which each generate a beam of 670 nm in the shape of a fan that spreads out by 20 mm by 1 mm with a divergence of 8.5 degrees (Burchell et al., 1999). The beams are then converted into a curtain shape. The first step is that they are directed onto a barrel lens which produce a wide beam. These beams are then passed through a slit to produce a curtain with a width of 5 mm and a depth of 1 mm. The projectile will then pass through both of these curtains, which are

a known 4.99 ± 0.1 cm apart. These curtains are then focused by another barrel lens into a photodiode, one for each curtain. The current from the photodiode is monitored via a trans-impedance amplifier, if there is a drop in the illumination being received by the trans-impedance amplifier then the output of the circuit rises. This creates a signal that is displayed on a digital oscilloscope. This can then be analysed very quickly by the operator after a shot, and due to the known distance we can calculate the speed of the projectile which is accurate within better than $\pm 1\%$ (Burchell et al., 1999).

The final chamber described in Burchell et al. (1999) is the target chamber, which is a cylinder 1 m long and 0.4 m in diameter. The entire backside of the chamber can be opened allowing for easy access and set up of targets, and full access to the electrical feedthroughs which permits the instrumentation of targets. Burchell (1999) then describe some of the more general features of the gun and its projectiles. For example, the projectiles can range from anywhere between 0.4 and 2.5 mm in diameter. These sizes have two determining factors, the 2.5 mm is the maximum size that at that time could be fitted in a sabot, hence that is the biggest projectile that could be fired, whilst the 0.4 mm is the smallest single object able to be placed on the central axis of the sabot consistently. These values have since changed, and sizes from 0.12 to 3-5mm can be fired today. The projectile can also come in a variety of materials such as: glass, nylon, cellulose acetate, ruby, aluminium, stainless steel and phosphorus bronze and are usually spherical or clouds of sub-millimetre objects fired (similarly to a buckshot) from the split sabot. As far as projectiles go however, if it can fit in a sabot then it can be fired, even if they are non-spherical such as rods or platelets. The gun can be fired up to 4 times a day during normal operation, and the speed obtained in the shot can depends on several factors: amount of gun powder, the mass of the piston and sabot, the nature of the gas and pressure raised to before firing and finally the strength of the bursting disc. By changing these parameters, the gun could fire at specific velocities in between 1.1 and 5.7 km s^{-1} , with 5.9 km s^{-1} being the highest velocity recorded at the time of (Burchell et al. 1999). Today the gun has a maximum speed of $8.4\text{--}8.6 \text{ km s}^{-1}$.

We can also see some of the data Burchell et al. produced at that time, comparing the variables that are changeable in the gun, thus affecting the speeds which can be reached with the light-gas gun. Shown in figure 2.8 is the effect pressure has on the

speed of the projectile, depending on the gas being used and in figure 2.9 we can see how the mass of the propellant affects the speeds attainable with the different accelerators also described in Burchell et al. (1999), which electronically accelerates sub-micron dust, where SP is single particle mm sized, BS is buckshot above 10 μm , P is fine grated powder (sizes down to a few μm in diameters) or different projectile types in the light-gas gun and VdG is the Van de Graaf accelerator.

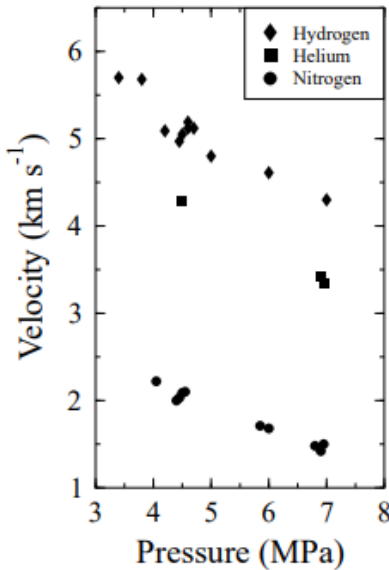


Figure 2.9: Comparing velocity with launch tube pressure for different light-gas propellants.

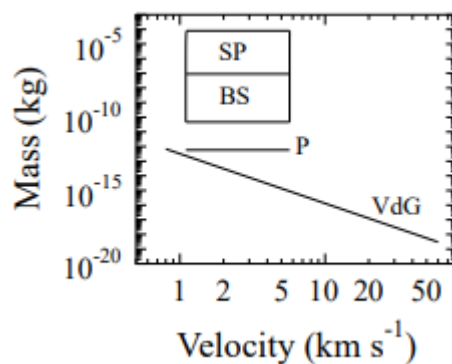


Figure 2.10: Comparing velocity with Mass of propellant and the ranges attainable with these varying methods. SP = Single particle (mm scale), BS = buckshot (above 10 μm), P = fine grated powder (sizes down to a few μm in diameter) and VdG = Van de Graaf accelerator.

2.4 Other Guns

In the early 2000's, E. Schneider and F. Schäfer, at the International EMI Fraunhofer Germany, published a paper 'Hypervelocity Impact Research – Acceleration Technology and Application'. Schneider and Schäfer (2001) highlights that hypervelocity impact experiments are crucial for simulating and studying meteoroid and orbital debris impacts on spacecraft and planetary surfaces. Furthermore, acceleration techniques need to be continually worked on and improved in order to experimentally cover as realistic a range of encounter velocities as possible and deliver input data and evaluation criteria for numerical hydrocode methods for impact simulations. Schneider and Schäfer go into a lot of detail on several different types of hypervelocity accelerators, here however we focus on what they have to say about light-gas guns, which they describe as a "most versatile instrument".

They mainly go into detail about how the gun functions, specifically how with the use of a compression piston, one can transfer the energy of a propellant combustion (such as a shot gun cartridge as seen in Kent) to a light gas such as hydrogen or helium in a pump tube. This compression produces high pressure until the diaphragm bursts and the hot gas can expand into the launch tube, where the projectile in it is sabot will be accelerated by the expanding gas a visualisation of this can be seen in figure 2.10. After the launch tube, the projectile separates from the sabot which hits a stopping plate, whilst the projectile passes through a central hole in the plate and then through a velocity measurement system before finally hitting the target. They quote Stilp, agreeing that the advantage of this method is the high speeds available potentially up to 10 km s^{-1} , and illustrates what happens in a useful diagram (figure 2.11).

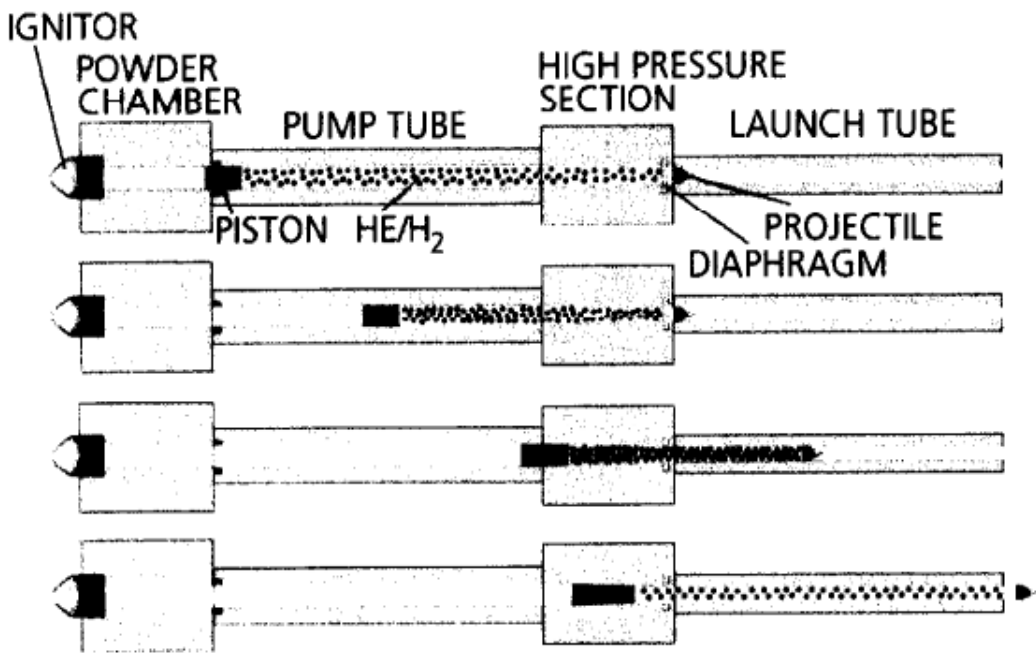


Figure 2.11: Visualisation of light-gas being used to propel a projectile. (Schneider et al. 2001)

One issue with the gun, described so far is that they fire horizontally. Such targets include sand or other low cohesion materials. The solution is a gun that can be mounted vertically. An example of a large gun of this type, the NASA Ames vertical gun. A compact light-gas gun in the ilk capable of firing at various angles is described in The Open University Planetary Impact Facility: A Compact Two-Stage Light-Gas Gun for All Impact Angles (McDonnell, 2006). As the name suggests, McDonnell goes into details about the development and installation of a light-gas gun at the Open University. What makes this gun unique in the UK, however is its ability to shoot in both the horizontal and vertical axis, not to mention several angles in between. Yet some targets cannot be mounted vertically (suitable for horizontal impacts).

The NASA Ames vertical gun range (AVGR) is similar to other light-gas guns, and is used to simulate high-speed, celestial body impacts on a small scale (nasa.gov, 2010). In 1966 the AVGR began operation, supporting the Apollo program, to better understand lunar surface geomorphology. As of today, the facility still providing data for NASA's Planetary Geology and Geophysics program. Similar to the light-gas gun at the Open University, the AVGR can at fire different angles from the horizontal in increments of 15 degrees, at velocities approaching 7 km s^{-1} . The projectile speed can vary from

anywhere from 0.5 – 7 km s⁻¹ with projectile sizes range from 0.005 - 7.6 mm, in different sized collections, i.e 1.5 - 7.6 mm were individual, the 0.2 – 1.0 mm were fired in groups of three and the 0.005 – 0.2 mm are grouped in clusters of many. The pressures reached in the impact chamber could range between 0.00005 – 1 Bar. Essentially the NASA Ames Vertical Gun Range is an older, larger, version of the gun developed at the Open university.

McDonnell (2006) describes a two-stage light-gas gun was designed by UniSpaceKent and constructed at the Open University. The gun was based on a 4.7 mm bore launch facility, supplied by Physics Applications International (PAI). This means there is a high mechanical rigidity under all angles of launch. Using an integral small target chamber of about 200 mm diameter or an intermediate planetary target chamber, the gun would be rotated through all the angles between horizontal and vertical as can be seen in figures 2.12 and 2.13. There was also the option of an even larger target facility which sits beneath the guns mezzanine location, and the gun would be moved horizontally and rotated to reach the facility; when using a set-up like this however, pre-set angles though vacuum ports are needed. Through the position of the axis of rotation, and some assistance from trim weight, the residual force moments can be balanced out. McDonnell (2006) then explains the choice behind a rotating gun; he agrees that most of the time a horizontal gun and vertical target are adequate for space impact studies, especially as in the beginning impact phase, gravity is inconsequential, and the convenience of access makes up for the additional costs and complexity that come along with it. However, for planetary applications a horizontal target in a vertical gravity field is often more useful because this copies the planetary environments we want to examine, and it allows for the presentation of both dusty and liquid target materials. Mounting these types of material vertical is impossible and under impact, gravity would have an extensive effect on the trajectory of the ejecta and its distribution. Therefore, a new design was evolved. The new design needed to serve two purposes: firstly, the “ready and reliable” aspect of the horizontal LIGHT-GAS GUN facility used at the University of Kent, and secondly the new planetary impact scenario (McDonnell, 2006).

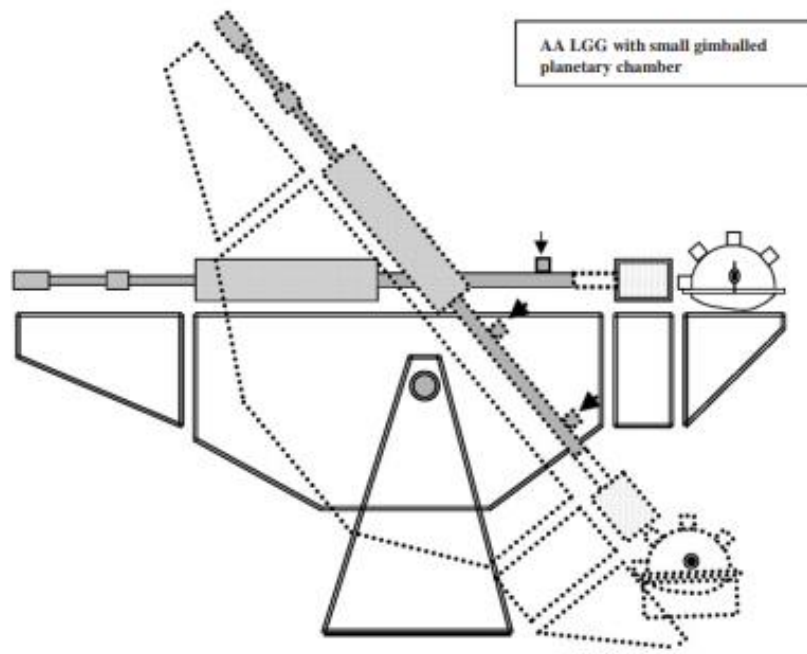


Figure 2.12: The Open University rotatable light-gas gun with a small gimballed planetary chamber (McDonnell, 2006).

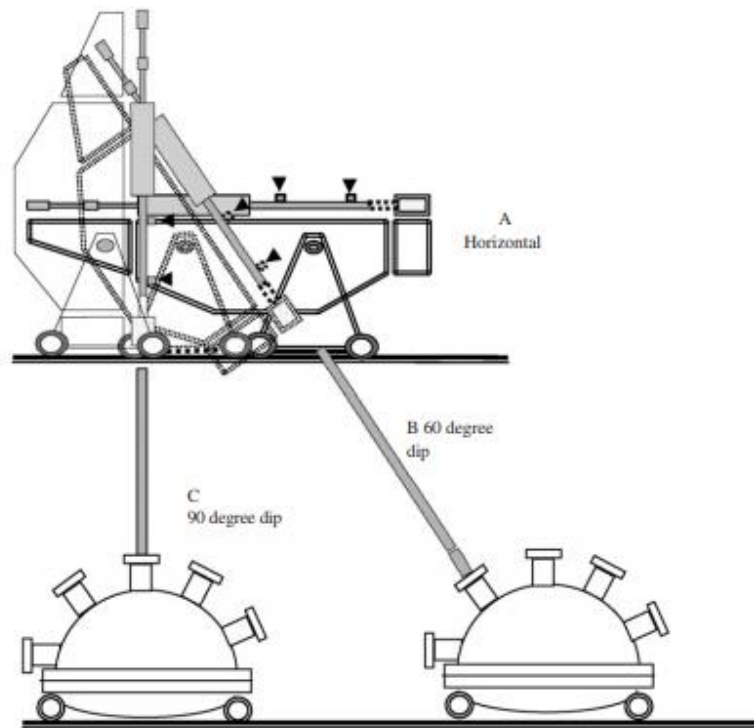


Figure 2.13: Deployment of the large planetary chamber, where both the gun and chambers are on rails, so that they can be accommodated for different launch tube lengths.

A new support rig was designed to complete this aforementioned task, by supporting the light-gas gun at a single point by a yolk. However, the strength that was needed for stability meant it was questionable whether the light-gas gun could be operated at various intermediate angles routinely. Therefore, this would be affected by two decisions, how big the facility would be (i.e. bore and length) and the velocity range that would be acceptable. Other light-gas guns at the time do not differ significantly in velocities reachable; once above 7 km s^{-1} the return on both capital and the recurrent costs becomes less and less making it less viable. Basically, parts wear out and break much faster as speed approaches 8 km s^{-1} . Similarly, the scale of the facility reaches a point where the return for the cost becomes unreasonable. The facilities size was kept in moderation. McDonnell argues “if there was already an existing requirement to extrapolate laboratory data from the centimetre scales to the planetary scale of 1000s of kilometres, then it could hardly be said to be significant whether the starting point was measured in millimetres or centimetres.” To get cm sized projectiles requires a much larger, heavier gun, larger recoil system, larger target chamber, isolated building (in case of misfire), longer time for cleaning the gun after shots , and so on. Due to this way of thinking, along with the needs of space materials study and planetary impact studies, there was need for dichotomy in the operational modes of this particular gun. For the space materials, a fast cycle time was needed to explore multi-parameter space such as velocity, projectile density or impact angle. Whilst, the planetary impact studies were going to require horizontal targets, large chambers and more extensive diagnostic equipment. The new specification was based on the PAI long-life unit gun, as used at the University of Kent. For the vertical configuration it would be necessary to have remote controls for gas filling, evacuation, firing and diagnostics and connected via an interface near the axis of rotation. Rotation about a single axis was desirable, as it could be positioned such that the facility could be balanced to reduce torques arising from the rotation. The resulting gun is shown in figure 2.12 and figure 2.13 and has been available for use for some years now.

2.5 Summary

In summary, over the years the average light-gas gun has slowly developed from a large, only horizontal, low-speed velocity accelerator in 1957, all the way to modern day light-gas guns, which can rotate from horizontal to vertical angles, can reach speeds previously unattainable, and fire projectiles, larger, smaller and of different shapes and materials, thus expanding the range of possibilities for experiments that can be undertaken in an effort simulate a wider range of environments and projectiles, to understand our universe. Later in the thesis, I will go into detail about a new vertical light-gas gun being developed at the University of Kent, that is as of writing, successfully firing at low-speed up to 0.9 km s^{-1} and will soon be functioning and ready to fire at speeds over 1 km s^{-1} .

Chapter 3: Methodology

3.1 Sand Target

As previously mentioned in past chapters, I decided to use sand as a target material. There were several reasons for this. That it is a non-cohesive material, that it does not collapse under the weight of gravity and that sand is a good material to use that can simulate planetary regolith. The fact that it is non-cohesive means that after being struck by a projectile, the sand will create a relatively large crater for me to examine. The fact that it does not collapse under gravity meant that I had plenty of time to run measurements on the crater; this would not have worked with a less stable non-cohesive material such as water. Finally, the fact that sand can be used to simulate regolith makes for interesting results, that we can then compare with different types of regolith such as from the moon or another planet.

I planned to be consistent with my experiments, using only one type of sand to get a series of relatable results. I did however, run one experiment with a different type of sand grain, to see the difference this would make to the cratering. I was careful to

make sure that the grains of the sand I used were a small size compared to the projectile. I must state explicitly that I am aware, that in a planetary hypervelocity collision, the ratio of projectile to regolith size often would be much greater than I am using in the laboratory. It was also important when making my target that the depth of the sand was not going to be too shallow, as this could have created problems upon impact; the shockwaves from the impact could have bounced off the base of my target and propagated back through the sand a second time, causing the crater to become altered.

The sand I used was made up of small grains. The bag had the code: BS 4550 PT5 Fraction D SD-0702-02/36 BS EN ISO 9002 1994. Part of the key identifying aspects of this code for the sand was the fraction letter. The fraction letter indicates the size and roundness of the grains that make up the bulk sand, D being very fine in the range of 0.3 – 0.5 mm, small grains and A being very coarse, relatively large grains in the range of 2 ± 0.5 mm. We made sure before each shot to bake the sand for an hour at 120 degrees Celsius to evaporate as much moisture as we could from the sand, making the target as consistent as possible.

Previous to my first shot, I investigated the sand, obtaining information about it. I measured the bulk density (ρ) by filling a container of known dimensions and weighing it. In my case I used a circular plastic box with a 137 ± 0.5 mm with a depth of 5 ± 0.5 mm. The box was placed on the scales, and they were reset to 0.0 g. The container was then filled with sand until the top, at which point excess sand was scraped off the top using a flat edge. The container was then weighed and came out to 60.6 ± 0.05 g. From the dimensions of the container we could find the volume of the sand using the equation:

$$V = \pi r^2 h \dots (3.1),$$

where V is the volume, r is the radius of the cylinder and h is the height of the cylinder. Using this equation, we found the volume to be equal to 0.074 ± 0.007 m³. This means we can use:

$$\rho = m/V \dots (3.2)$$

Where ρ is the bulk density, m is mass and V is volume. From this, we can find the density of the sand, which came to be equal to $822.2 \pm 7.4 \text{ kg m}^{-3}$. We then had to investigate the frictional coefficient of the sand. To do this we used a device to measure the angle of inclination of a box of sand as I tipped it. I then recorded two points: when the sand begins to move a few grains, and when the whole of the sand begins to slide. For the sand I was using, this happened at 22.1 ± 0.1 and 24.9 ± 0.1 degrees respectively. We then had to calculate the frictional force acting on the sand, which can be broken up into two components F_{parallel} and $F_{\text{perpendicular}}$.

$$F_{\text{parallel}} = mg \sin (\theta) \dots (3.3)$$

$$F_{\text{perpendicular}} = mg \cos (\theta) \dots (3.4)$$

Where m is mass, g is acceleration due to gravity and θ is the angle of inclination. We can then combine these two to get the overall frictional force:

$$F = \tan (\theta) \dots (3.5)$$

Therefore, the coefficient of friction for the sand I am using is between 0.406 ± 0.01 and 0.464 ± 0.001 respectively.

For my second shot, I used a different type of sand at the same speed as the previous shot, to determine what effect this would have on the crater. Later in the paper, I discuss these differences. This second type of sand was labelled: BS 4550 PT5 Fraction A SA-0702-02/95. The fraction A indicates the relative largeness and coarseness of the sand. A comparison between the two different fractions can be seen in figure 3.1 below.

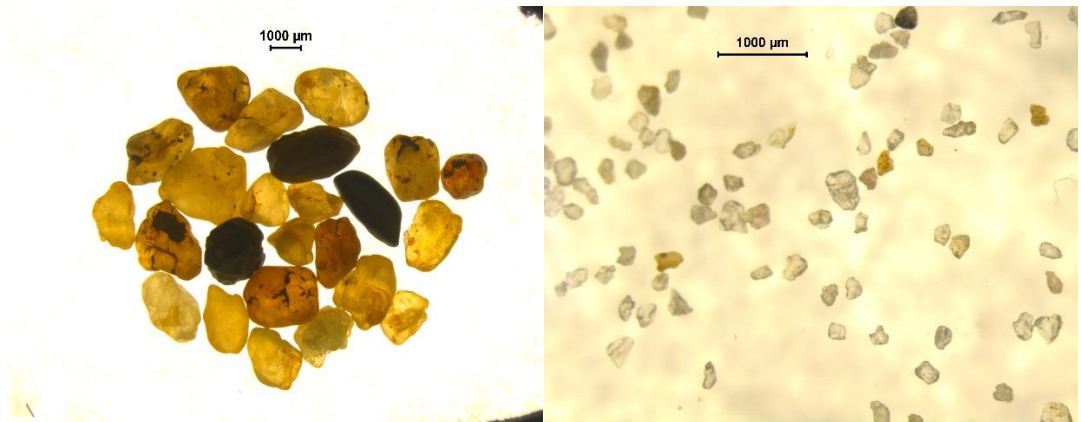


Figure 3.1: Comparison between two different Fractions of Sand. Fraction A pictured Left, Fraction D pictured Right.

As with the other sand I measured the bulk density, volume, mass and frictional coefficient of the sand. First, I packed the sand into a container of known dimensions, in this case it was a plastic cube 50 ± 0.5 mm by 50 ± 0.5 mm by 35 ± 0.5 mm. From this information and the formula for finding the volume of a cube I could, calculate the volume of the sand I would be using:

$$V = L^2 h \dots (3.6),$$

Where V is volume, L is the length of the equal sides and h is the height of the cube. From this I found the volume to be equal to $(8.75 \pm 0.15) \times 10^{-5} \text{ m}^3$. I then weighed the sand in the box to find the mass, this came out to 146.2 ± 0.1 g. Then from the volume and mass we can use equation 3.2 to find the bulk density. The density was found to be equal to $1670.9 \pm 29.2 \text{ kg m}^{-3}$. Then as with the previous sample of sand, I found the frictional coefficient. From the method I used I found that sand began to move at 35 ± 0.5 degrees and it all began to move at 40 ± 0.5 degrees. From equations 3.3-3.5 we can find out the frictional coefficients which are 0.70 ± 0.01 and 0.84 ± 0.01 respectively.

Once all the macro measurements had been made, it was time to move onto the measurements of the individual sand grains. I began with Fraction D sand. First I collected grains onto a plastic dish and placed them under the laboratory microscope, and photographed them. I repeated this several times so as to get as much data as possible on the sand grains. In figure 3.3 we can see a collection of the sand grain images I took. I then used a software (QWIN, supplied with the microscope by the

manufacturer) device, to enter the magnification, and draw perpendicular lines across each sand grain, measuring their lengths and widths. I collected these into a table and was able to use equation 3.7 to find the eccentricity of each grain:

$$e = a/b \dots (3.7),$$

where a is the radius of the ellipse one way, b is the radius of the ellipse perpendicular to a , where a is the smaller of the two lengths and e is the eccentricity of the sand grain, which is a measurement of how circular the grain is. From this we can gather the data and compare how the size of the sand grain affects the eccentricity of the grain. The results can be seen in figure 3.2. The areas of each grain is in terms of pixels on the image. Since no use has been made in this work of the absolute grain sizes, the data were not converted to absolute qualitative. The eccentricity ranges from 0.3 – 1.

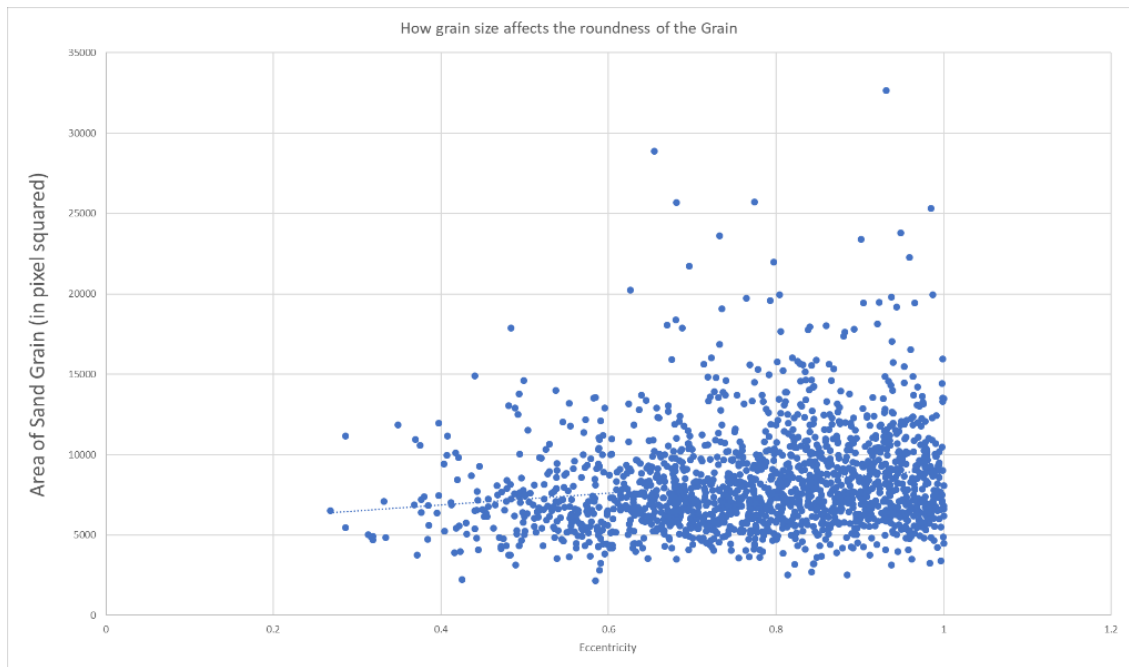


Figure 3.2: Graph of Area of a sand in arbitrary units against the eccentricity of the sand grain.

I repeated a similar process with the second grain type Fraction A. An image of these grains is in Figure 3.4.

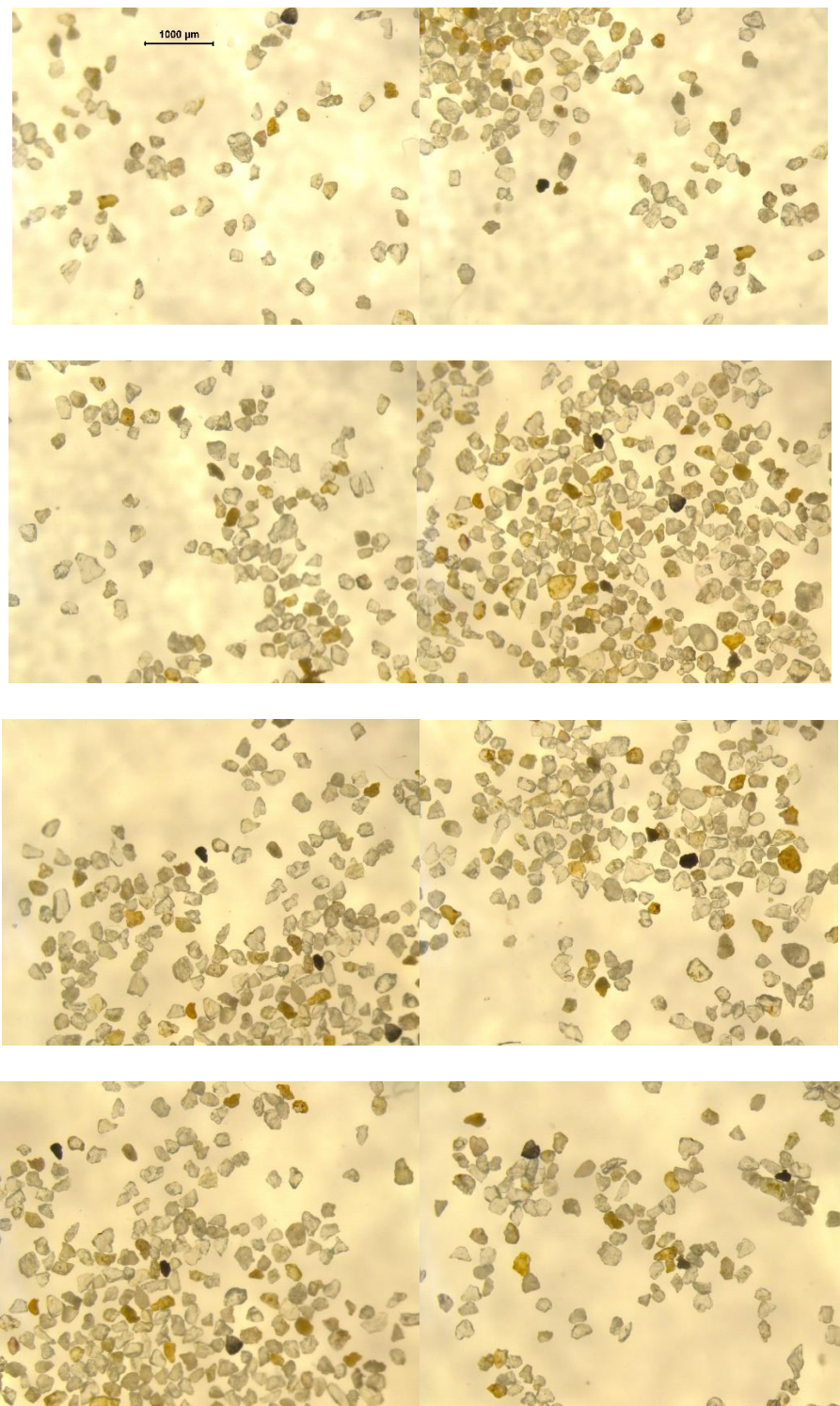


Figure 3.3: Images of Sand grains under microscope for fraction D sample taken at 2x magnification.



Figure 3.4: Image of sand grains from Fraction A sand, used for measuring grain dimensions.
Shown under Microscope at 0.71x Magnification.

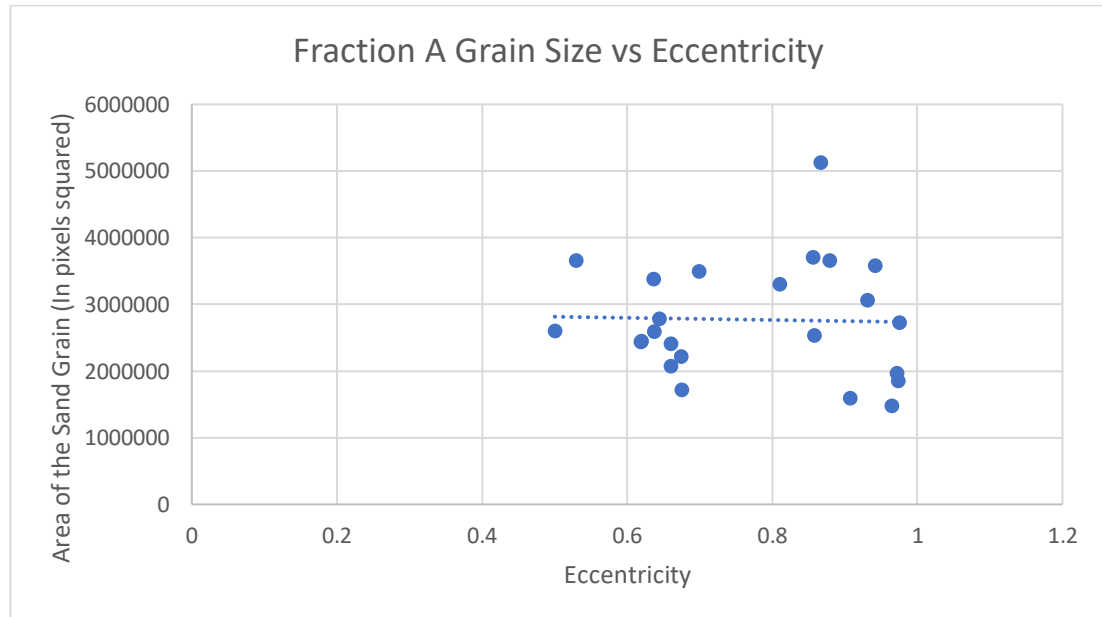


Figure 3.5: Graph of Fraction A grain area (in an arbitrary unit) vs Eccentricity.

As we can see from figure 3.2 most the fraction D sand grains are around the same size, the majority lay between $5000 - 10000 \pm 10$ units and of those grains, most lie between $0.6 - 1 \pm 0.004$ in eccentricity. Whilst the fraction A sand grains have less data, we find $0.6 - 1 \pm 0.004$ in eccentricity.

Now that I had measured the parameters of the materials I would be working with; the next step was to create my target. This was a fairly simple process and produced a crude yet, very effective target for my shots. First, I found a plastic bucket which had a diameter of 22.0 ± 0.1 cm and a depth of 16.0 ± 0.1 cm. I made sure to use a bucket with enough depth that, when shot, the vibrations through the sand would dissipate before reaching the bucket, as if they do not they can bounce back off the interior wall of the bucket and back through the crater a second time, disturbing the crater shape and rendering the results unreliable. With a diameter of 22.0 cm and a depth of 16.0 ± 0.1 cm the volume of the bucket is found using equation 3.2. From this equation we find the maximum volume is equal to $(9.50 \pm 0.07) \times 10^{-5} \text{ m}^3$. I found two of the buckets with the same measurement.

Next I took the sand and I baked it in the laboratory for 1 hour in a Thermo Scientific VT6060P oven, at 120 ± 3 degrees Celsius (uncertainty found from: https://assets.thermofisher.com/TFS-Assets/LED/brochures/Vacuum%20Ovens%20Portfolio%20Brochure_FINAL_Aug2017.pdf).

This process removed any excess moisture from the sand, helping to make a more accurate repeatable process with reproducible results. I filled one of the buckets with the sand from Fraction A and the other bucket with the sand from Fraction D. I filled both to the top and made sure to hit the sides and bottom of the buckets to make the sand compacted slightly and was too loose. This means the sand grains fill their ideal packing fraction and again make the process more reproducible. There are anecdotes in laboratories of groups getting different sized craters in sand on a result of not doing this and allowing the target to settle. I then to the best of my ability made sure the top of the sand was level, smoothing slightly with a ruler. Once that was done my target was ready.

3.2 Setting Up the Gun

The next step after making my target was to ask Mike Cole the Experiment Officer, to set the gun for a shot. This was easier said than done, as the title of this thesis says, the gun is still a prototype and at the beginning of my experiments was still under development and had not yet been fired successfully. During my time working on this project, I acted as a spare pair of hands for Mr. Cole. I assisted him with several small tasks, that contributed to the gun being suitable for operation. One task was developing a constructing a safety barrier for the gun, and another was designing and constructing a guide for the foot of the gun as can be seen below in figure 3.6, so that the cables would not get entangled when lifting. I also simply observed a lot of the development of the gun. This helped in the general development of my mechanical skills.

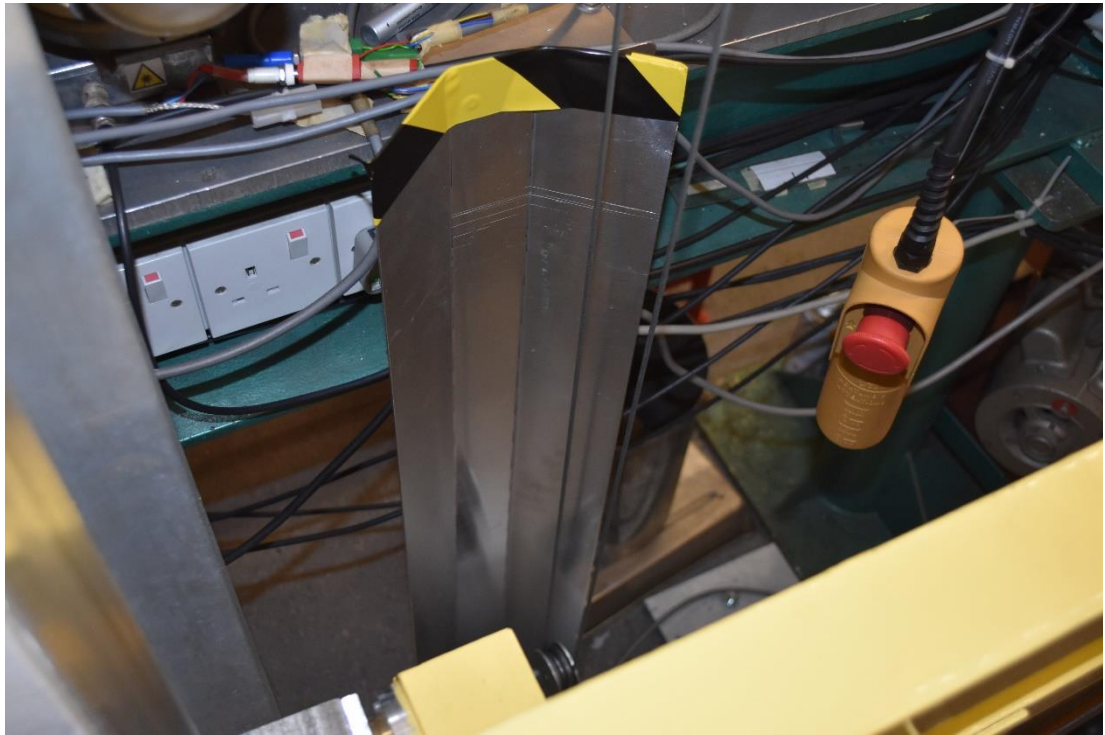


Figure 3.6: “Foot Guard” developed and built by me, in an effort to avoid the cabled for the lift becoming entangled with the wires connecting the electronics in the lab.

In the beginning, one of the main problems the development work had to overcome was an accurate aiming system for the gun. Mr. Cole experimented with a laser pointer, designed for horizontal gun aiming, but this unfortunately did not work for the vertical gun design. He tried several different methods of aiming before he developed the idea for a mirror on the interior of the blast tube, the mirror would have a hole cut in the centre and be sized to match the dimensions of the blast tube it was attached to the rear of. He then marked the mirror with a black marker, producing a black cross on the mirror with the hole the projectile would fly through at its centre. When this tube would then be installed, a light could be placed under the exit point for the projectile and it would reflect off of the mirror and shine back down into the blast chamber, producing a cross with a central dark spot marking the area the projectile would fall into. Using this cross the tube could be moved through tightening and loosening straps attached to the side of the tube to keep it steady during the kickback of the gun. By tightening and loosening these cables the cross can be moved slightly, meaning we could now aim the projectile to where we wanted it to be.

The next obstacle was a velocity measurement system that could be installed safely inside the blast tank. Mr. Cole decided to design and construct a collapsible rig that could be placed in the blast tank. This rig would hold a metal box with an access hole at the top and exit hole at the bottom. It would be placed flush with the top of the blast tank, the hole in the top lining up with the exit from the blast tube. Inside metal box was a metal unit containing a cylindrical hole throughout the centre for the projectile to pass through, lining up with the blast tube above and the target below. To the left and right of this tube were compartments to place light gates in. There were four compartments, two on each side of the tube, one on top of each other. Each of the left compartments contained the producer of the light gate and each on the right side was the receiver. When the projectile passed through the central tube, it would pass through both light gates sending a signal to the oscilloscope in the laboratory, allowing for accurate time of flight measurement. MR. Cole measured the distance between the light gates as 119.5 ± 0.5 mm. He used a ruler which would have had an accuracy of ± 0.5 mm however due to the fact that the gates are non-parallel

beams, the true value should be taken as 119 ± 1 mm. The details of these mechanisms can be seen in figure 3.7 – 3.10 below.

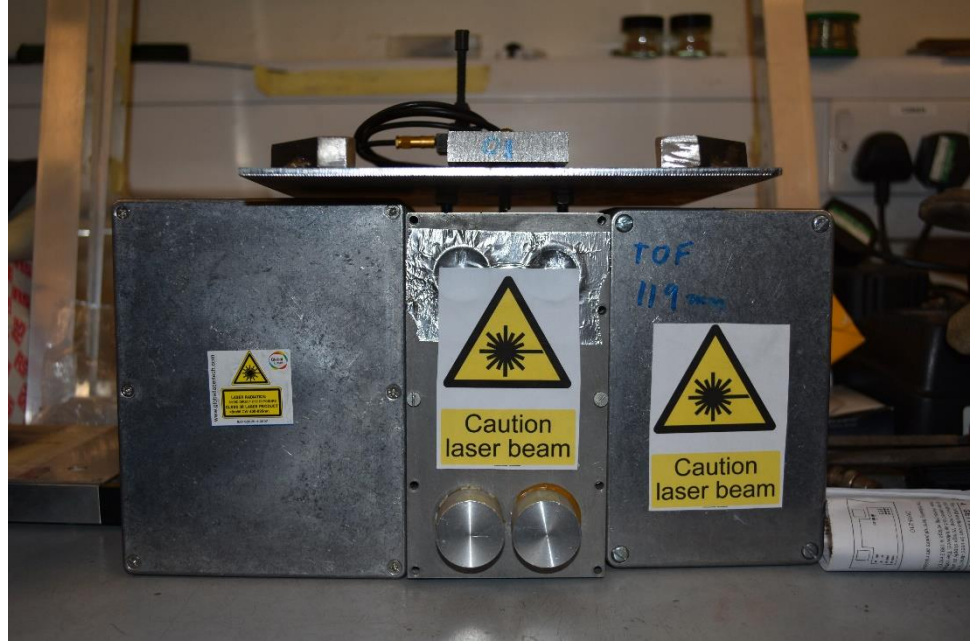


Figure 3.7: The box that gets placed inside the blast tank, containing the light gates, to measure the velocity of the projectile.



Figure 3.8: Top of the velocity measurement system, the blast plate is visible, placed on top to catch the sabot, so only the projectile velocity is measured. Behind the hole is a tube for the projectile to travel through before the target, during which it passes through two light-gates for velocity measurement.



Figure 3.9: The exit of the velocity measurement system, where the projectile leaves the system to then move on to the target.



Figure 3.10: The velocity measurement system, on top of the rig set up in the blast tank. A metal box sits on top of the entrance to the system in an effort to stop the projectile or sabot ricocheting and interfering with the target.

Mr. Cole also developed an electrical lift system for the gun seen in figure 3.11, so that it could be safely constructed on the ground seen in figure 3.12 before being lifted and fitted over-head. To the position seen in figure 3.13, this is where my barrier came into play, making sure no one could walk underneath the gun while it was over head. Once these two main obstacles had been overcome, the gun was ready to be tested. The gun now acted in a very similar manner to the horizontal gun, except the projectile was held in a vertically downwards blast tube, and the horizontal light-gas pump tube would fire into an L-shaped corner component, shifting from a horizontal direction of motion to a vertical one. It would then accelerate the projectile downwards. I feel it necessary here to specify that although there would be an acceleration affect from gravity in the downward motion of the projectile, the effect it would have on the projectile during the time of flight between the second light gate (the point of velocity measurement) and the target is negligible, and we can take the speed thought the light gates as the speed of the projectile on impact.



Figure 3.11: The lift used to safely move the constructed launch tube from the ground up above to where it needs to be fitted for a vertical shot.

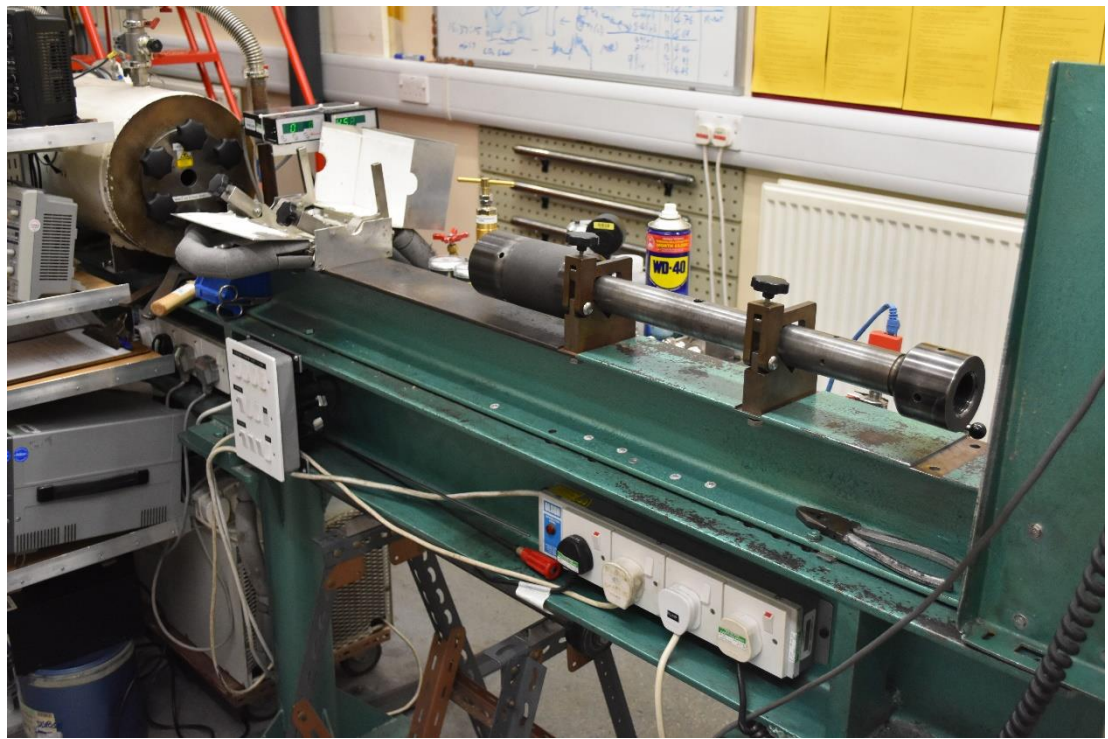


Figure 3.12: The area where for a regular horizontal shot, the launch tube would be set-up, however in my case it was where the launch tube was set-up before being moved up high to for the vertical shot.

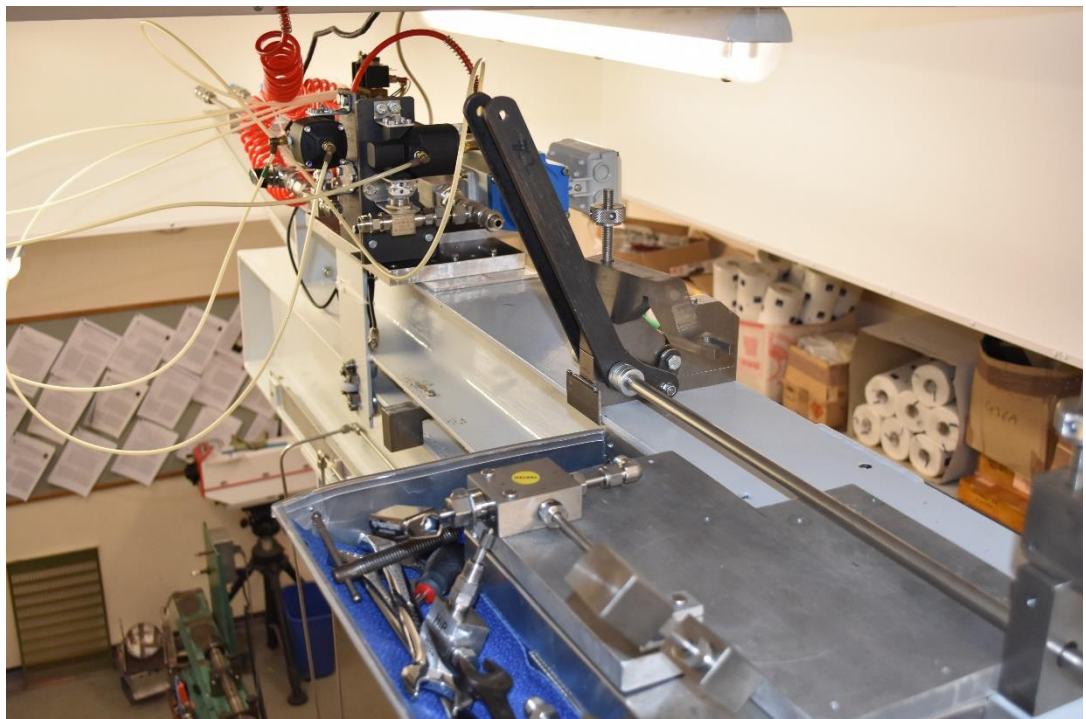


Figure 3.13: Area where the launch tube, post being set-up, would be placed before being tied into the rest of the system. In the back visible, is the beginnings of the mechanisms for the above 1 km s^{-1} shots being prepared.

An important step to the firing of the gun, was placing the projectile in a sabot before launch, this sabot would separate from the projectile and hit a blast plate, before the projectile passes through into the blast tank. We used a 4-way 0.170" sabot to hold our 1 mm 420-AISI-Steel ball bearing. An image of a sabot is placed below in figure 3.14.

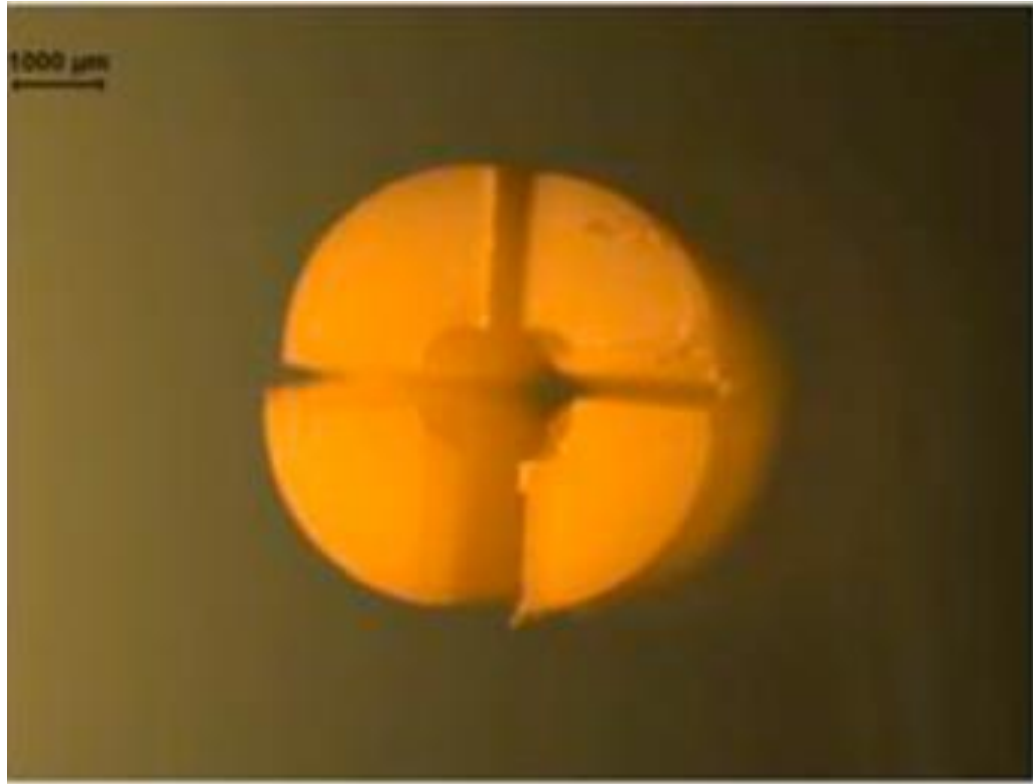


Figure 3.14: A split sabot, this shows how the four interlocking sections fit together around the projectile in the centre. (Hibbert et al., 2017)

Our first attempt to fire took place on the 19/10/2017 and unfortunately was not a success. There was a small gas leak limiting the speed of the projectile and the projectile then hit the blast plate, not reaching the target. However, after re-alignment of the gun, a second shot was attempted on the 24/11/2017. The re-alignment involved producing a metal target plate for the target to sit on, with a large cross-hair on it, that we could fix to the base allowing for the target to be accurately placed in the same place, each time a shot was taken. The second attempt was a success. Hydrogen gas was used. The Fraction D sand was used as a target, with a (1 ± 0.1) mm 420-AISI-Steel ball used as a projectile. The pressure in the pump tube before the 4-way 0.170 inch sabot fired was (83 ± 1) bars. The speed of the shot was then calculated using the

known distance between the light gates (119 ± 1) mm and the time of flight, shown by the distance between the two electrical signals from the light gates, shown on the oscilloscope. In this case the time of flight was shown to be (141 ± 1) μs . This gave a velocity of 0.844 km s^{-1} . Table 3.1 shows the full results for this and the following successful shots, taken during the year.

<i>Shot #</i>	<i>Date</i>	<i>Sabot Type</i>	<i>Target Material</i>	<i>Projectile</i>	<i>Vacuum 1 (mbars)</i>	<i>Vacuum 2 (mbars)</i>	<i>Gas</i>	<i>Pressure in the pump tube (bars)</i>	<i>Time of Flight (μs)</i>	<i>Calculated Velocity (km/s)</i>
1	19/10/2017	4-Way .170"	Fraction D	420-AISI-Steel Ball 1 mm	0.24	0.23	H	N/A	N/A	N/A
2	22/11/2017	4-Way .170"	Fraction D	420-AISI-Steel Ball 1 mm	0.44	0.43	H	83	141	0.844
3	23/11/2017	4-Way .170"	Fraction A	420-AISI-Steel Ball 1 mm	0.22	0.21	H	82	135	0.881
4	01/02/2018	4-Way .170"	Fraction D	420-AISI-Steel Ball 1 mm	0.19	0.19	N	52	364	0.327
5	10/05/2018	4-Way .170"	Fraction D	420-AISI-Steel Ball 1 mm	0.22	0.21	Kr + N	77	412	0.289

Table 3.1: Collective result data from the successful shots taken with the vertical gun between the dates 19/10/2017 and 10/05/2018.

Once I had completed a successful shot, the next step was to measure and collect data on the craters left in my targets.

3.3 How to Measure

During each shot, the target chamber was evacuated to approximately 0.5 mbar therefore, the first step after a shot was to let the vacuum return to room pressure. This would typically take around 10 – 15 minutes, after that we could open the blast tank door. This blast tank is the same blast tank used for the horizontal gun, spoken about in previous chapters. Then I would then take pictures of my target still in the tank, so as to make sure I kept records of the crater before there is any chance for disruption. I would place a ruler for reference and take several images of the crater, attempting to collect as much data as I could before moving the crater. Examples of these images can be seen in figures 3.15 – 3.19.



Figure 3.15: Image taken of shot 2 after impact, still in the blast tank, before being moved. Smaller craters can be seen where the fragments of the material. The ruler scale is in cm.

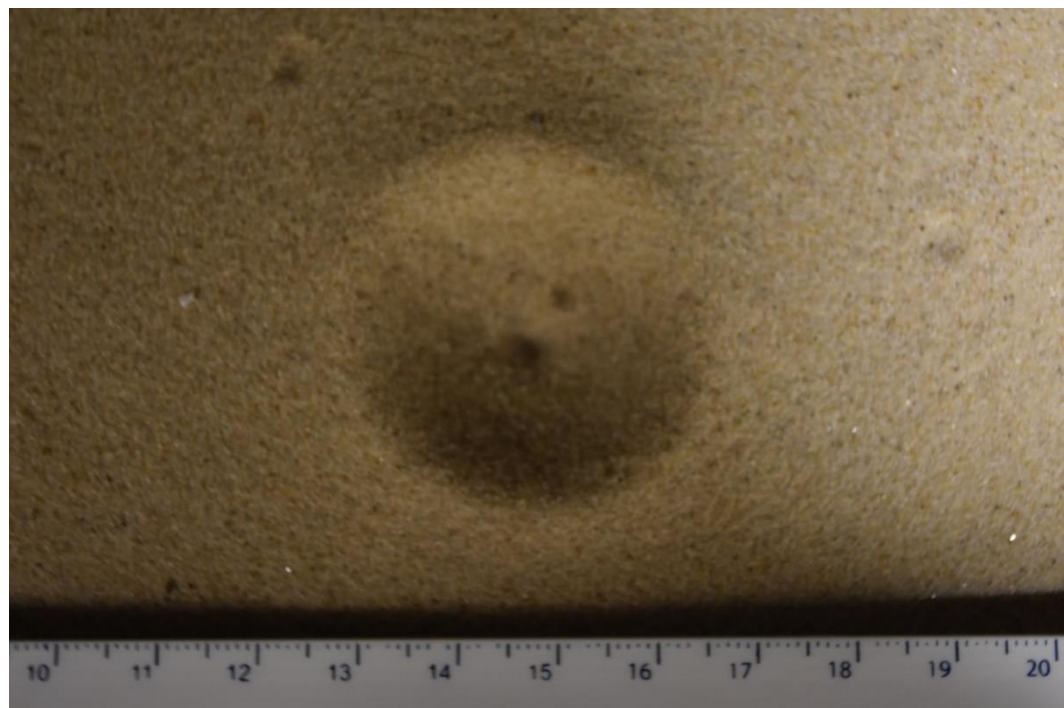


Figure 3.16: Close-up photograph of the crater taken before being moved from the blast tank. From this distance it is possible to measure the crater diameter crudely, with an accuracy of ± 3 mm.

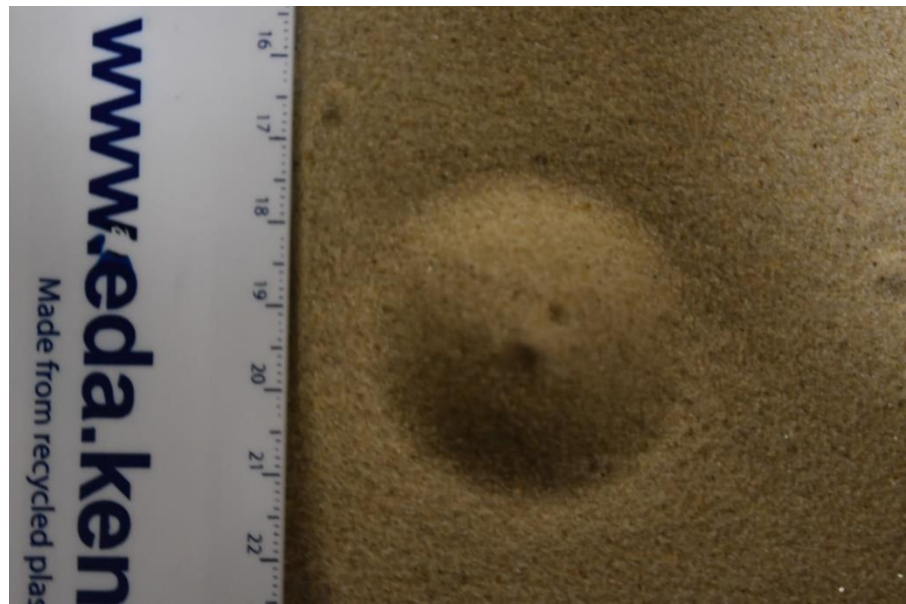


Figure 3.17: Second close-up photograph taken of the crater before being moved from the blast tank. The ruler has been rotated 90 degrees so as to measure the crater perpendicular to the original measurement; this allows for us to measure the eccentricity of the crater. Again from this distance the diameter crater can be crudely measured to an accuracy of ± 3 mm.



Figure 3.18: Another photo was taken slightly further back but in the same vein as figure 3.16. This image however was to allow for averages to be taken of the measurements, reducing the error in them.



Figure 3.19: Yet another image was taken, as close as could be done, inside the blast tank, with the ruler as close as possible without disturbing the crater. This produces an image from which a diameter of the crater can be measured to a higher accuracy of ± 1 mm.



Figure 3.20: Images of the blast plate was also taken in an effort to measure the distance the sabot split away from the projectile and to see if it was an even separation. From this distance, a measure of the amount the sabot parts separated can be measured to an accuracy of ± 1 mm.



Figure 3.21: Another measurement of the split sabot was taken, perpendicular to the original measurement, this allows for measurement of the evenness of the sabot split.

It was important to collect as many images as possible, so as to avoid missing any details of the crater, and to keep a complete record of the process. Below is a collection of several images all taken in part of analysing the craters, these images represent a process that was repeated for every crater produced. See from Figure 3.20 and 3.21 what a good sabot separation looks like.

Once the crude measurements have taken place, I removed the target from the blast tank into another room, where I had set up a system for measuring the depth of the crater. This method involved using a Vernier calliper with a needle on the end of it. This can hang vertically above the target on a solid bar, the needle point and the length of the Vernier calliper can pass through a slit in the bar so that it can be elongated so as to just touch the surface of the sand. The bar also has a ruler perpendicular to it, meaning I can take depth measurements every (1 ± 0.5) mm. The depth measurements are taken using a Vernier calliper set to zero at a point of my choosing, after that each measurement is either $+/$ - my zero point. Each measurement is taken to an accuracy of ± 0.05 mm. The Vernier callipers themselves are more

accurate than this with an accuracy of ± 0.005 mm. However the reproducibility during measurement rounds this error up to an effective 0.05 mm. Images of my set-up and method can be seen in figures 3.22 – 3.25.

By measuring the depth and along a line across the centre of a crater, I can measure the diameter and shape of the crater more accurately than with a ruler. In effect, by measuring the placement of the highest point on the crater, and recording the distance between the two points, this makes for a measurement with an accuracy of ± 1 mm.



Figure 3.22: A wide shot of my depth measurement set-up.

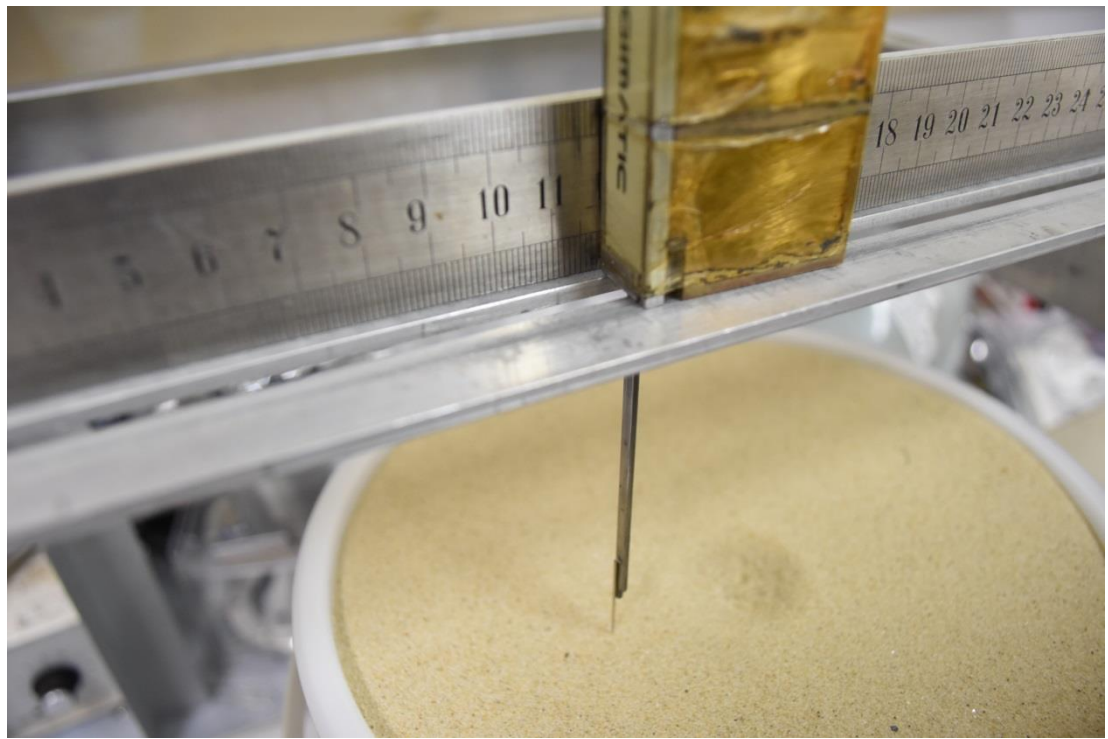


Figure 3.23: Image of depth and distance measurement set-up for measuring the crater depth and diameter of my target.



Figure 3.24: An image of the Vernier calliper's electronic readout, the Vernier callipers have an accuracy of ± 0.005 mm, however this gets rounded up by my human error to ± 0.05 mm.

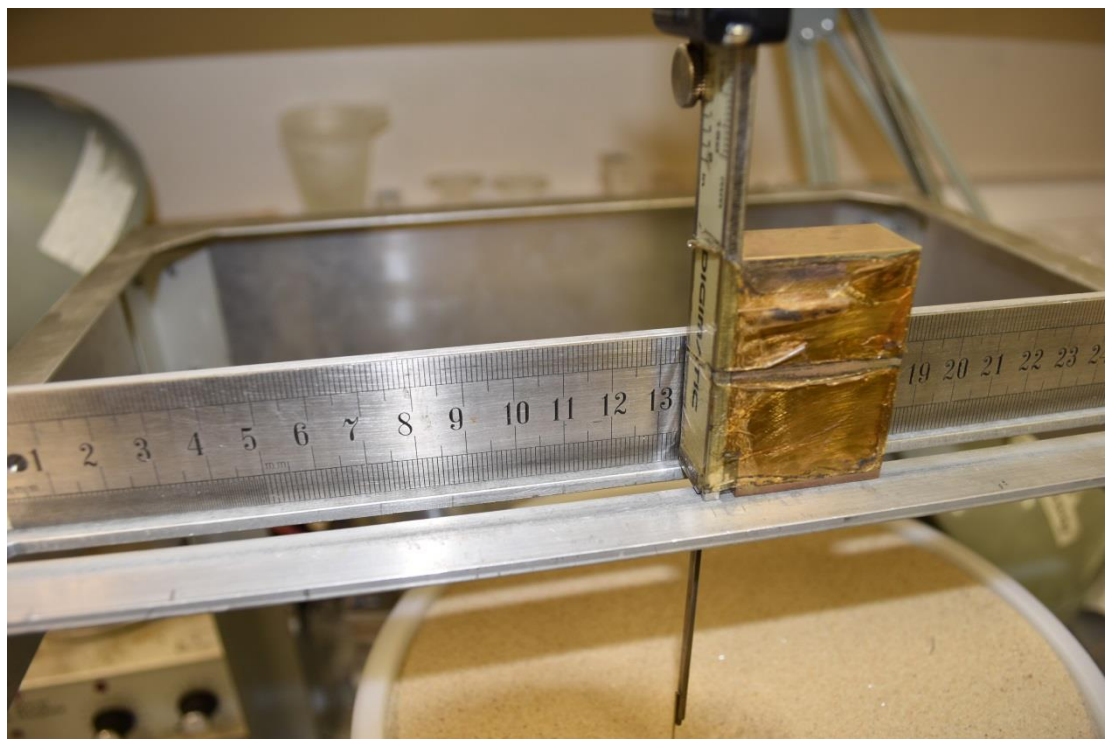


Figure 3.25: An image taken, showing how I could measure the distance of the increments of measurements I was taking. I would measure the depth every 1 ± 0.5 mm.



Figure 3.26: Another example of the preliminary crude measurements I would take of the craters, soon after impact, before it is moved. This is an example of the Fraction A sand.

Once I had collected and recorded my data, I then organised them into tables, looking at the relationship between the speed of the projectile and the diameter of the crater. I then investigated using pi-scaling with my data and comparing the results to those previously found by H. J. Melosh in his book ‘Impact Cratering’ (Melosh, 1989). I talk about this in more detail in the next chapter.

3.4 Error calculations

Throughout my paper I have indicated errors in the recording and results I have been detailing. In this section I want to go in to detail into how these errors are calculated and applied. Firstly, error usually stems from natural error in making a measurement. For example, reading a distance on a ruler, or the accuracy of a set of scales. In the case of the ruler, although the accuracy of the ruler itself is ± 0.5 mm, a more conservative estimate to the accuracy can be taken as ± 1 mm due to human error in taking a measurement with a ruler. In the case of scales, or an electronic readout, you usually take the last significant figure and add an error of ± 0.5 the last significant figure, for example, a readout of 0.01 g on an electronic scale would have an error of 0.01 ± 0.005 g.

Then comes the error in calculated values, for example, when I measured the size and height of a container, to calculate the volume. There are a set of formulas relevant for this kind of calculations see table 3.2:

$Z = A + B$	$(\Delta Z)^2 = (\Delta A)^2 + (\Delta B)^2$
$Z = A - B$	$(\Delta Z)^2 = (\Delta A)^2 + (\Delta B)^2$
$Z = A * B$	$((\Delta Z/Z)^2) = ((\Delta A/A)^2) + ((\Delta B/B)^2)$
$Z = A / B$	$((\Delta Z/Z)^2) = ((\Delta A/A)^2) + ((\Delta B/B)^2)$
$Z = A^n$	$(\Delta Z/Z) = n * (\Delta A/A)$
$Z = \ln(A)$	$\Delta Z = \Delta A/A$
$Z = e^A$	$\Delta Z/Z = \Delta A$

Table 3.2: Relations between the formula for calculating a value and the formula for calculating the error in a value from the errors in the component values.

As seen in table 3.2, there are specific ways to calculate the error in a value given how the value is calculated and the errors in the component values. A good example of this is from calculating volume.

$$V = \pi r^2 h \dots (3.1)$$

From this formula we find the relationship between volume, radius and height of a cylindrical container. To find the error in the volume calculated, we need to first make sure we have the error in the radius measurement and the height measurement, Δr and Δh respectively. In my case Δr and Δh are equal at ± 0.5 mm, because they were measured with a ruler that had 1 mm increments. Combine this with table 3.2, we can use the relations from $Z = AB$ and equation 3.1 to calculate the error in V .

$$(\Delta V/V)^2 = (2\Delta r/r)^2 + (\Delta h/h)^2 \dots (3.8)$$

We know the values of Δr , r , Δh , h and V , meaning that the only unknown is the value ΔV . From equation 3.8 we can rearrange for ΔV . Which upon doing, we find that ΔV is equal to ± 0.007 mm³. As you can see from the calculations, error is not as simple as adding together the errors of the component values.

For each value in my paper, I follow these methods, either applying an error to a measured value, based on the method of measurement, or by using the formulas from table 3.2 to calculate an uncertainty for a calculated value.

3.5 Summary

In this chapter I have gone over why I chose to use a sand target, how I made the target and increased my reproducibility of measurements. I went into details about the calculations involved for making sure everything was within error parameters and calculating different variables I would need later. I looked in depth at the sand I decided to use and talked about why I chose the sand I did. I explained the procedure for using the light-gas gun, and the problems initially faced with the prototype vertical light-gas gun. I detailed my initial successful shots, and how I handled the results and

how I took my measurements and gathered my data. I then briefly explained how I calculated the errors in my results. Next, I will be talking about my results and analysis.

Chapter 4: Result Analysis

In this chapter I will go into details about the results I collected from my series of experiments during my time with the University of Kent. I break down the individual data I physically collected, and how and what I used this information to calculate. I will present the graphs I produced with this information, which includes cross sections of the individual craters produced by the light-gas gun and comparative graphs showing the changes with the craters with variables such as speed and density. I explain and utilise the method of pi-scaling to my craters and then finally compare my results with those produced in the past by Melosh in his book *Impact Cratering: A Geological Process* (1989).

4.1 The Shots

During my experiments, I was able to record 5 successful shots. There were on the 22/11/2017, 23/11/2017, 01/02/2018, 10/05/2018 and 13/09/2018. I have compiled the data from the shots into Tables 4.1 and 4.2. In Table 4.1 and 4.2 the crater number has 2 entries (The value before the decimal indicates which shot the crater belongs to, while the value after the decimal denotes whether it was the first measurement or the second measurement, which was the same crater rotated 90 degrees):

Crater Number	Crater Diameter (D) (m)	Volume (V) (m ³) measured	Volume (V) (m ³) Calculated
1.1	0.034	1.80E-06	2.92E-06
1.2	0.031	1.80E-06	2.92E-06
2.1	0.036	1.50E-06	5.31E-06
2.2	0.033	1.50E-06	5.31E-06
3.1	0.028	8.00E-07	1.47E-06
3.2	0.026	8.00E-07	1.47E-06
4.1	0.026	1.10E-06	9.66E-07
4.2	0.024	1.10E-06	9.66E-07
5.1	0.04	1.80E-06	2.82E-06
5.2	0.043	1.80E-06	2.82E-06

Table 4.1: Table depicting the dimensions of the crater dimensions after the shot was taken.

Crater Number	Velocity (v)(m/s)	Target density (kg/m^3)(ρt)
1.1	0.844	822.19
1.2	0.844	822.19
2.1	0.881	1670
2.2	0.881	1670
3.1	0.327	822.19
3.2	0.327	822.19
4.1	0.289	822.19
4.2	0.289	822.19
5.1	0.796	822.19
5.2	0.796	822.19

Table 4.2: Table showing the data for the speed of the shot taken and the density of the target material.

The data were collected from the depth measurements I took on each individual crater, as detailed in the previous chapter. These measurements allowed me to produce a virtual plot of a cross section of the craters, including both the original crater transection, and another plot of the same crater rotated by 90 degrees. Once the data were collected I had to make some alterations to the graphs, which involved finding the original level of sand from my data, creating a track line and finding the equation of this line, substituting in the x-values from my data, and using this to calculate new y-values for my data, this method makes the graph treat the line $x = 0$ as the original flat level of the sand in the bucket, meaning the crater depth can be easily measured and it makes the graphs more consistent and easier to measure and compare. These can be seen in figures 4.1 -4.10. In each case, the depth profiles pass through the centre of the crater. The profiles thus show a crater diameter (two per crater). The crater diameter is defined as being from the peak of one side of the crater to the peak of the other. These graphs give two values for the diameter of each crater. If perfectly circular, the diameter of each crater would be equal to within the measurement error. In table 4.1 it can be seen the values typically differ by 2 – 3 mm, that is by about 8 – 10%. The crater depth is found similarly, measured from the original surface plane. Again 2 values are given and can be seen to differ per crater and can be seen to differ by 0.1 – 2 mm, i.e a difference of 0.08 – 1%.

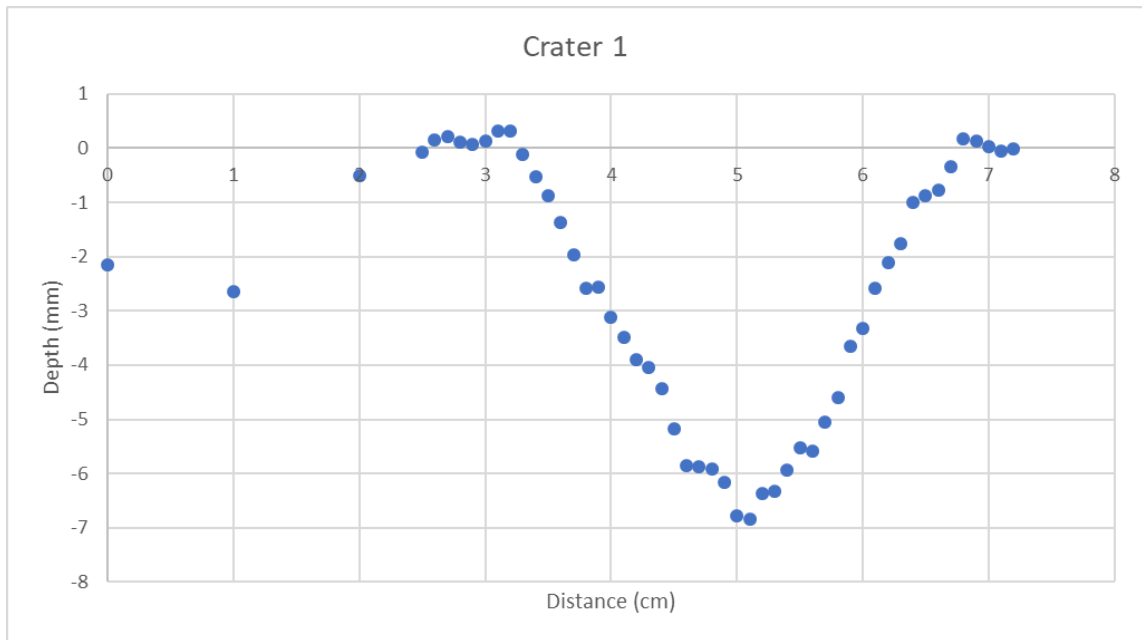


Figure 4.1: Crater 1, fired 22/11/2017 at a speed of 844 m s^{-1} into Fraction D sand.

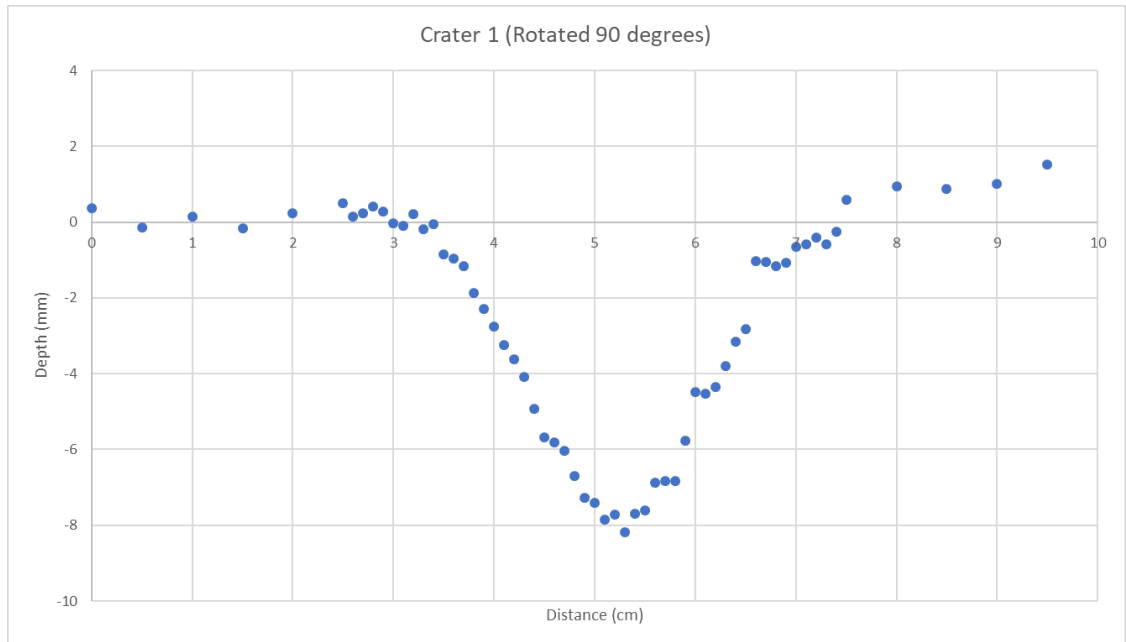


Figure 4.2: Crater 1, rotated 90 degrees, fired on 22/11/2017, fired at 844 m s^{-1} into Fraction D sand.

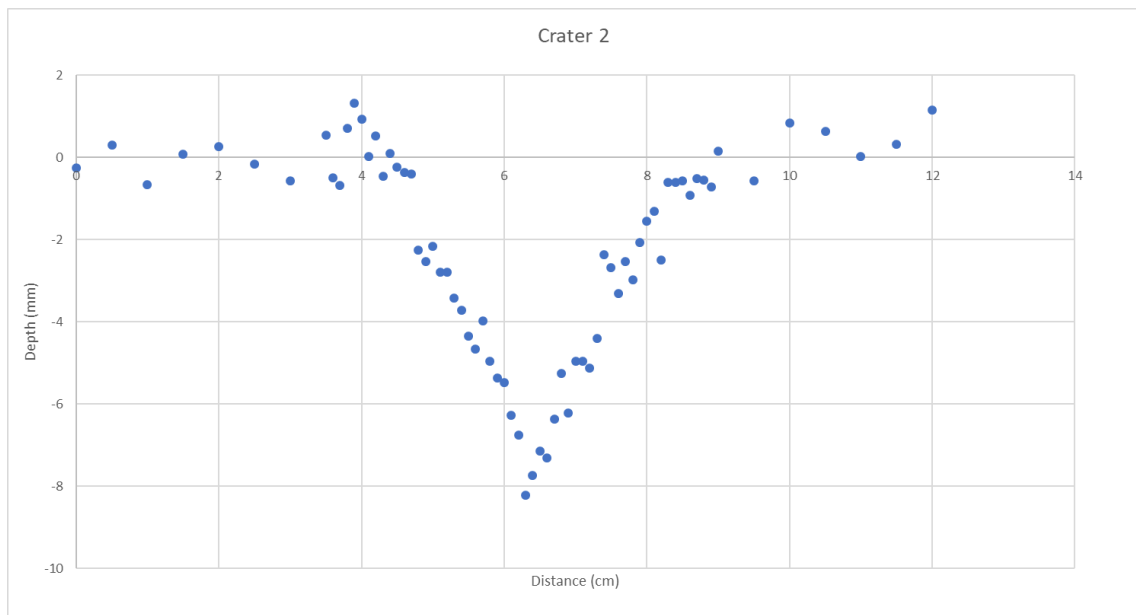


Figure 4.3: Crater 2, shot on the 23/11/2017, shot at a speed of 881 m s^{-1} into Fraction A sand.

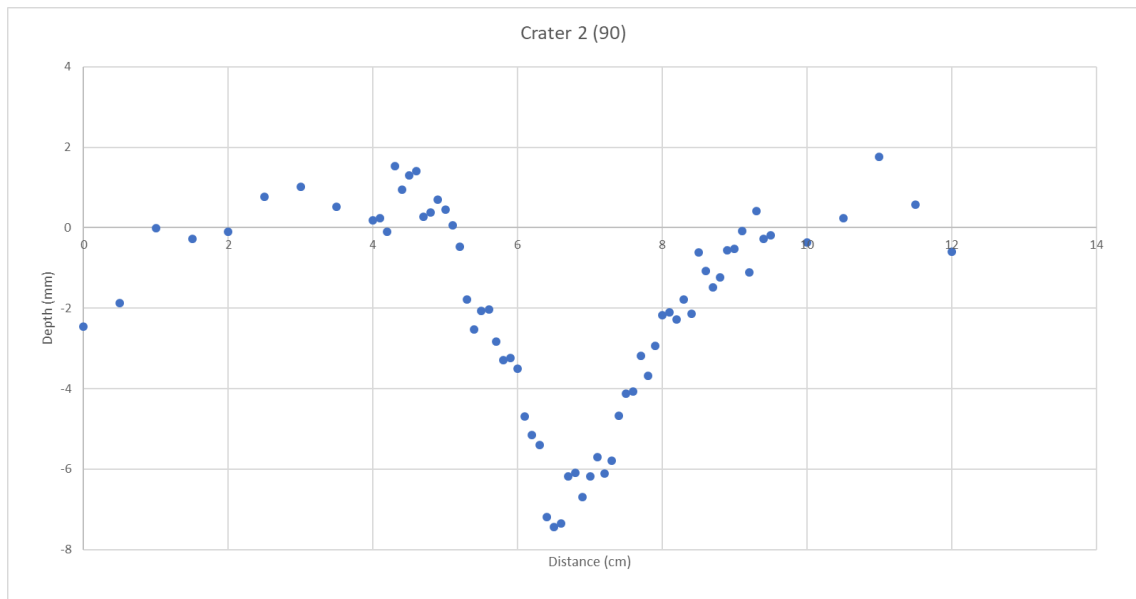


Figure 4.4: Crater 2, rotated 90 degrees, fired on 23/11/2017, fired at a speed of 881 m^{-1} into Fraction A sand.

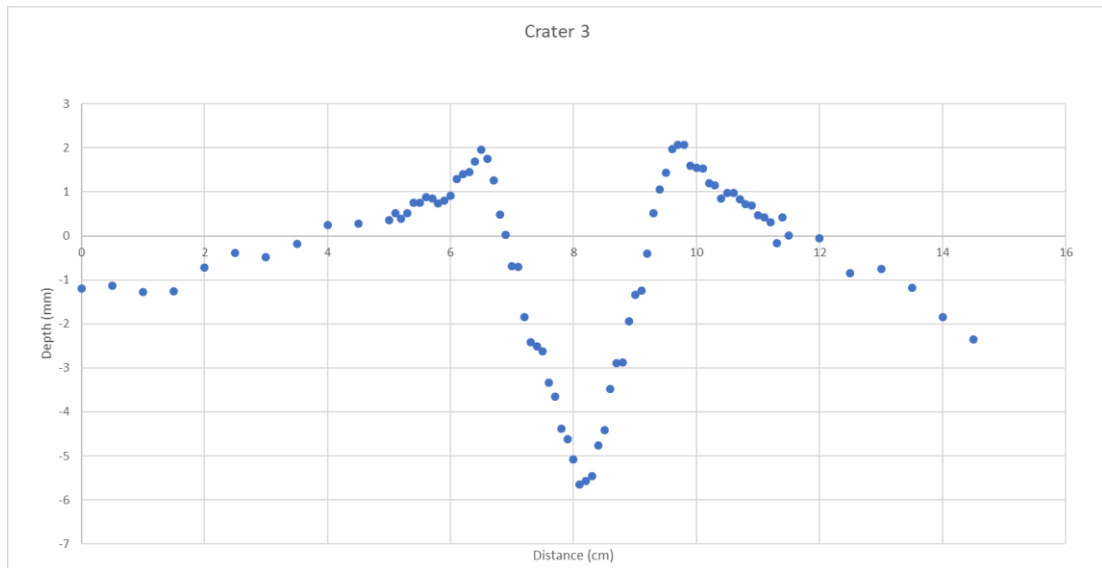


Figure 4.5: Crater 3, fired on 01/02/2018, at a speed of 327 m s^{-1} into Fraction D sand.

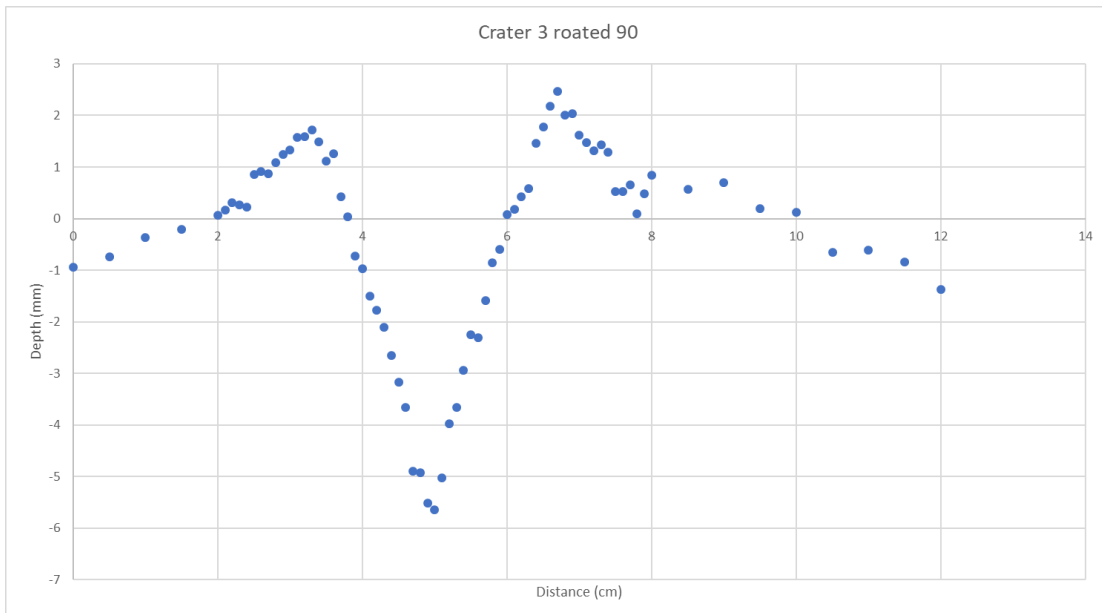


Figure 4.6: Crater 3, rotated 90 degrees, fired on 01/02/2018, at a speed of 327 m s^{-1} into Fraction D sand.

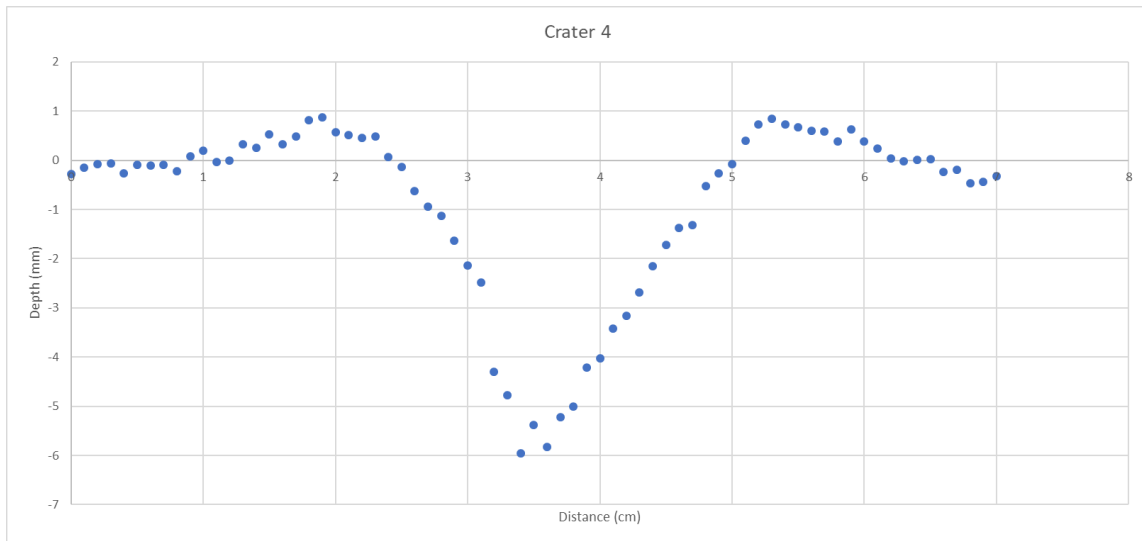


Figure 4.7: Crater 4, fired on 10/05/2018, at a speed of 289 m s^{-1} into Fraction D sand.

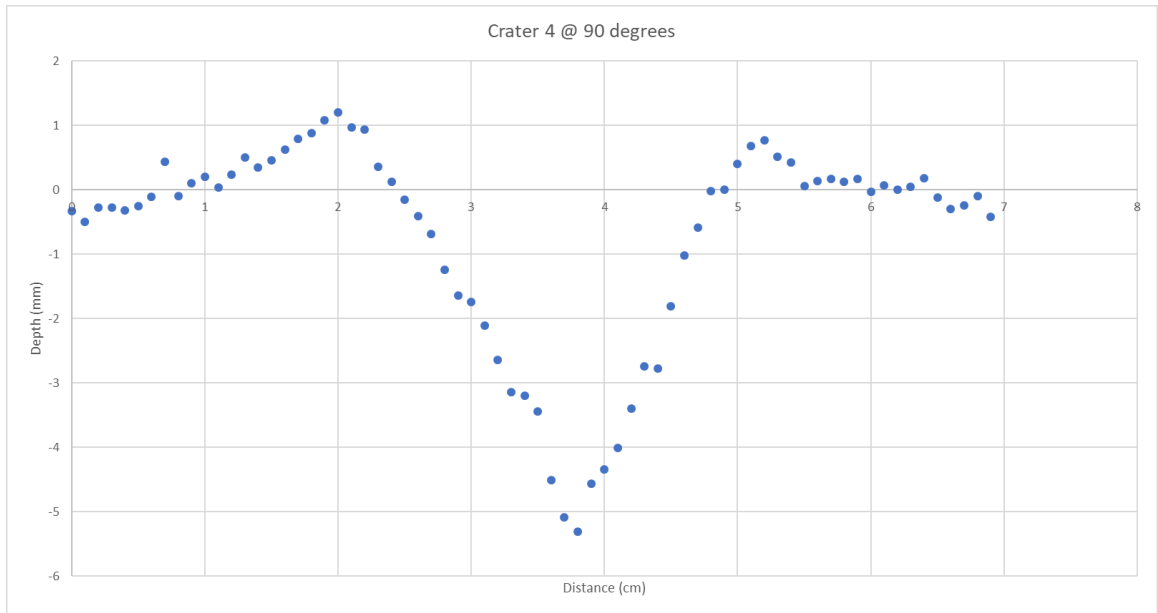


Figure 4.8: Crater 4 rotated 90 degrees, fired on 10/05/2018, at a speed of 289 m s^{-1} into Fraction D sand.

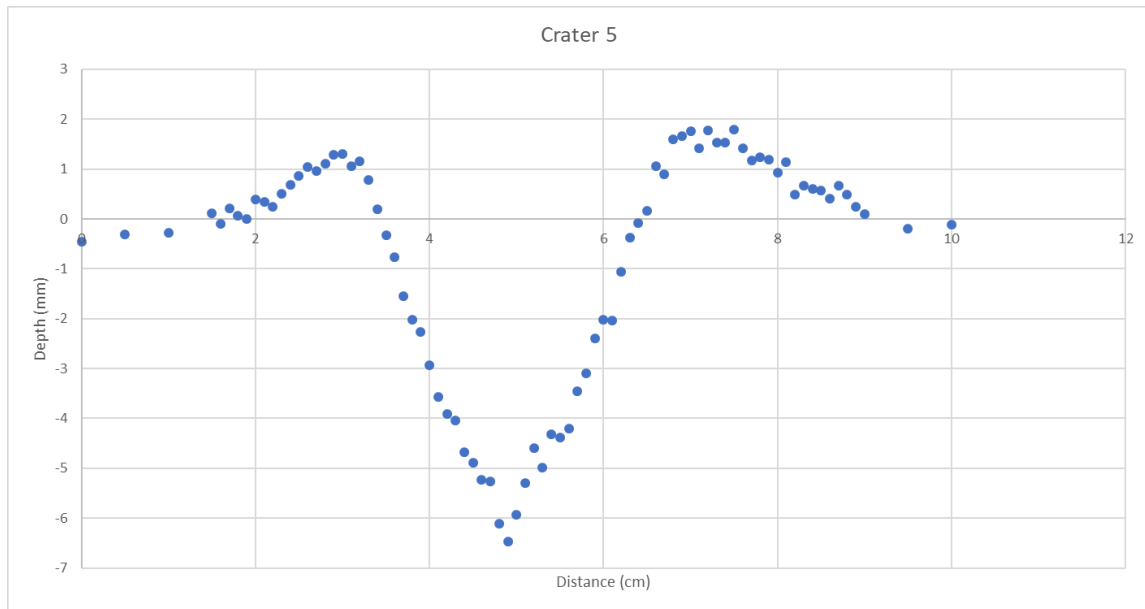


Figure 4.9: Crater 5, fired on 13/09/2018 at a speed of 796 m s^{-1} into Fraction D sand.

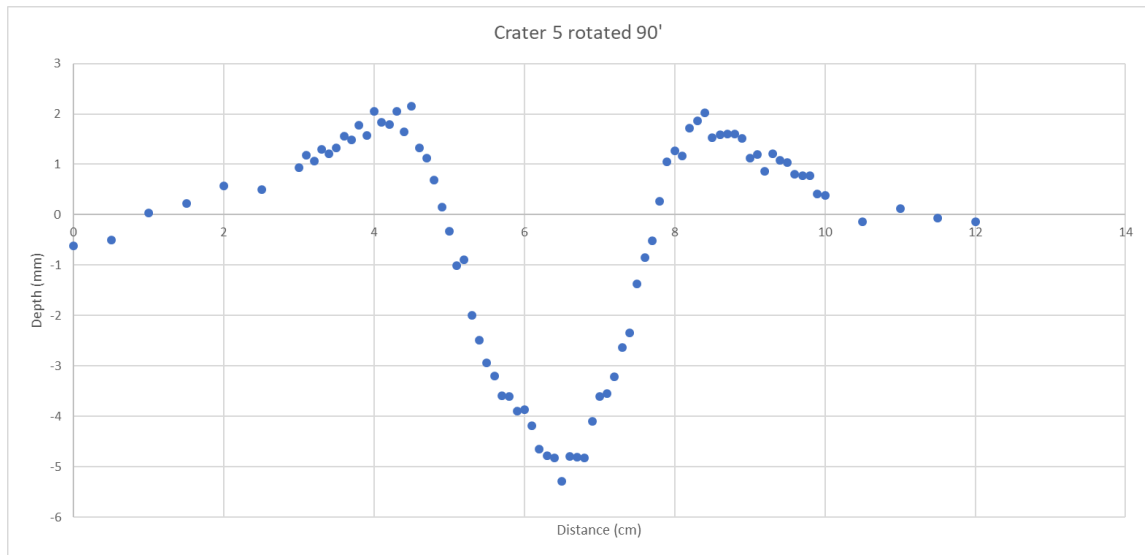


Figure 4.10: Crater 5 rotated 90 degrees, fired on 13/09/2018 at a speed of 789 m s^{-1} into Fraction D sand.

As can be seen in table 4.1, there are two measurements recorded for the volume of each crater. This is because I used two different methods to record the volume of the craters. One method ('measure') was to fill the crater with sand until it returned to its original level and record how much sand I had used in m^3 . The other method ('calculate') was to calculate the volume from the data I had recorded. Basically this split the craters into a series of small cylinders and recording each of the individual

volumes of these cylinders and adding them together. These two methods are recorded as ‘Volume measured’ and ‘Volume calculated’ in table 4.1 respectively. These values are the basic size parameters for the crater.

4.2 Pi-Scaling

One problem with doing lab experiments is that everyone does them slightly differently, i.e with different projectile types and sizes etc. Also, the size scales are very different to those for planetary scale impacts. A method is therefore needed to allow us to combine all this data and to extrapolate to different scales. The method favoured in the impact community is called pi-scaling. This is based on the method originally devised by E. Buckingham in 1914 (see Melosh, 1989). It is a type of dimensional analysis, wherein the parameters of a crater formation such as diameter, velocity, density, volume and projectile mass are combined into a series of dimensionless parameters. Some parameters rely on others and these can be determined experimentally and the dependence established.

The diameter of the crater (D) can be determined as a function of several factors, i.e:

$$D = F(v, \rho_p, \rho_t, Y, g, m), \dots \quad (4.1)$$

where F is the function, v is velocity of the projectile, ρ_p is the projectile density, ρ_t is the target density, Y is the target strength, g is gravity, and m is the mass of the projectile. All these values can be boiled down to relying on mass, length and time, and F must have the same dimensions as D , so therefore D can be treated as being a function of three dimensionless ratios:

$$\pi_1 = D * (\rho_t/m)^{1/3} \dots \quad (4.2)$$

$$\pi_2 = (1.61 * g * L) / (v^2) \dots \quad (4.3)$$

$$\pi_3 = Y / (\rho_p * v^2) \dots \quad (4.4)$$

$$\pi_4 = \rho_t / \rho_p, \dots \quad (4.5)$$

where L is the projectile diameter and π_D is a dimensionless ratio of the crater diameter. It can also be related to the ratio between the crater diameter and the projectile diameter:

$$\pi_D = 1.24 * ((\rho_t / \rho_p)^{1/3}) * (D / L) \dots (4.6),$$

which is an alternate form of equation 4.2. π_2 is called the “gravity-scaled size”, which is the other main dimensionless quantity we will look at. Furthermore, the volume of a crater can also be expressed in this way:

$$\pi_V = \rho_t * V / m \dots (4.7),$$

To begin with, I used the π method to make predictions for the possible outcomes of my planar shot programme. Using these dimensionless ratios, we can predict the size of a crater if we have a few key known values and see if data is scaling with strength π_3 or gravity π_2 . I used some values from my own experimental set-up, before my first shot, including the projectile size, density and mass, and the density of the target I was planning to use. I then used Diameter and Volume constants (C_D and C_V) that were found experimentally in past work. I obtained these from the Impact Cratering book (Melosh, 1989, Table 7.1), reproduced below in Table 4.3:

Target Material	Diameter Constants		Volume Constants	
	C_D	β	C_V	γ
Water	1.88	0.22	2.1	0.65
Quartz Sand	1.4	0.16	0.4	0.49
Ottawa sand	1.68	0.17	0.24	0.51
Competent Rock	1.6	0.22	0.2	0.65

Table 4.3: Experimental power law scaling constants. (Source Melosh, 1989)

This relies upon the relationships between the π terms which are given by:

$$\pi_D = C_D * \pi_2^\beta \dots (4.8)$$

$$\pi_V = C_V * \pi_2^\gamma \dots (4.9)$$

I made two tables, one using the Quartz sand constants and one using the Ottawa Sand constants as a function of impact speed. Combining this data, I could make a

prediction of how the crater in my experiment was going to look, based on speed, and how this speed was going to affect the diameter and volume of the craters. These predictions can be seen in figures 4.11 – 4.14. Furthermore, Melosh in his book, produces a log-graph comparing the two dimensionless values of π_D and π_2 . This ‘scaling’ is shown in Figure 4.15. The data for Ottawa sand and Quartz sand are taken by Melosh from Schmidt (1980) and Schmidt and Housen (1987) who used projectiles of aluminium and polyethylene with diameters 2.7 and 0.9 mm respectively with speeds in the range of 1 - 7 km s⁻¹. It can be seen that the two types of sand give roughly similar results which involve significantly smaller craters than in solid rock or water. Since my work uses a specific limited set of parameters, I have reproduced the curves of Figure 4.15 specific to my kinematic regime in Figure 4.16.

4.3 Previous Work

Once the predictions had been done, it I took my results and the data I have recorded, and combined it into its own table, calculating the π_D , π_2 and π_V values from my own experiments using equations 4.2, 4.3 and 4.7.

Quartz Sand Predictive Model

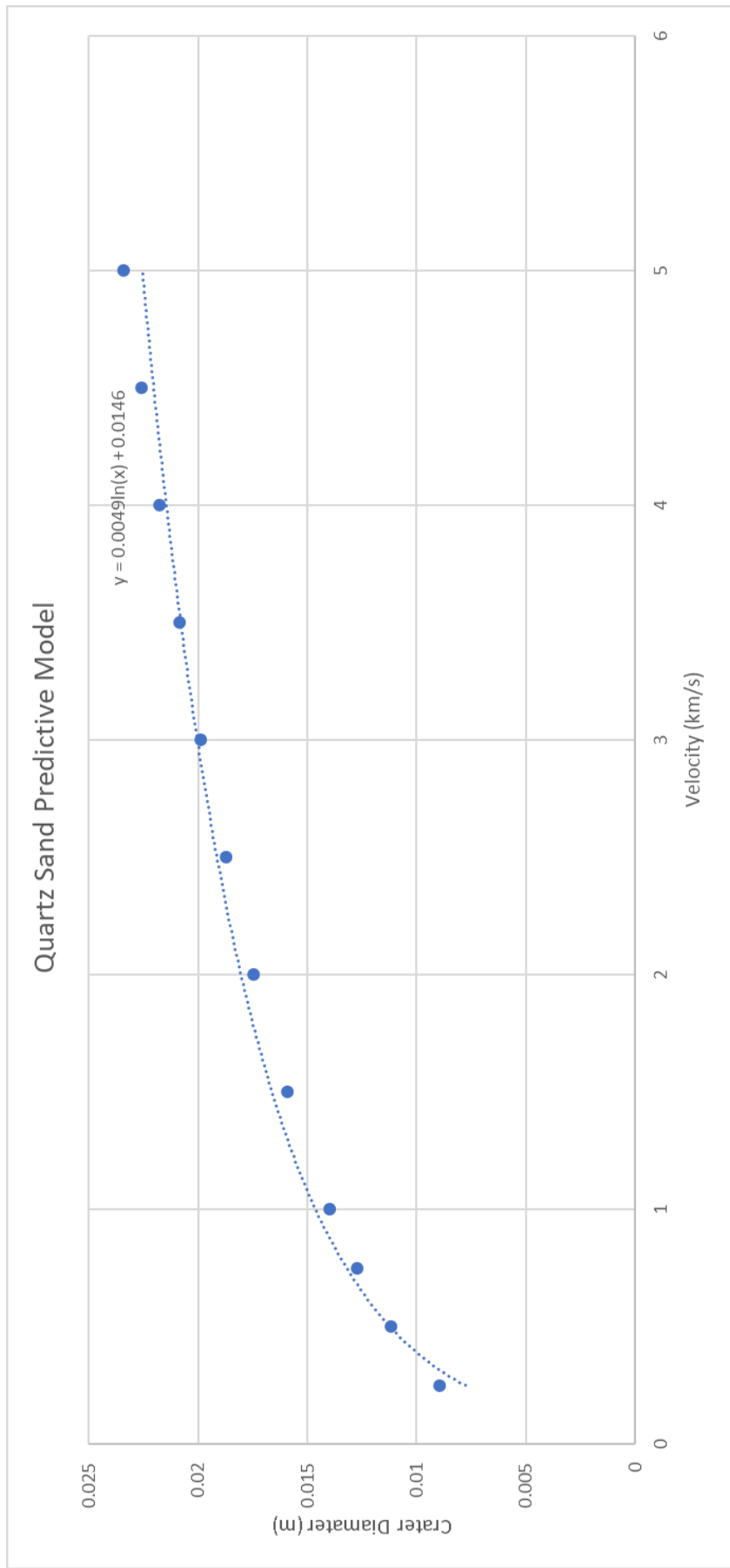


Figure 4.11: Predictive model of crater diameter vs velocity (Quartz Sand).

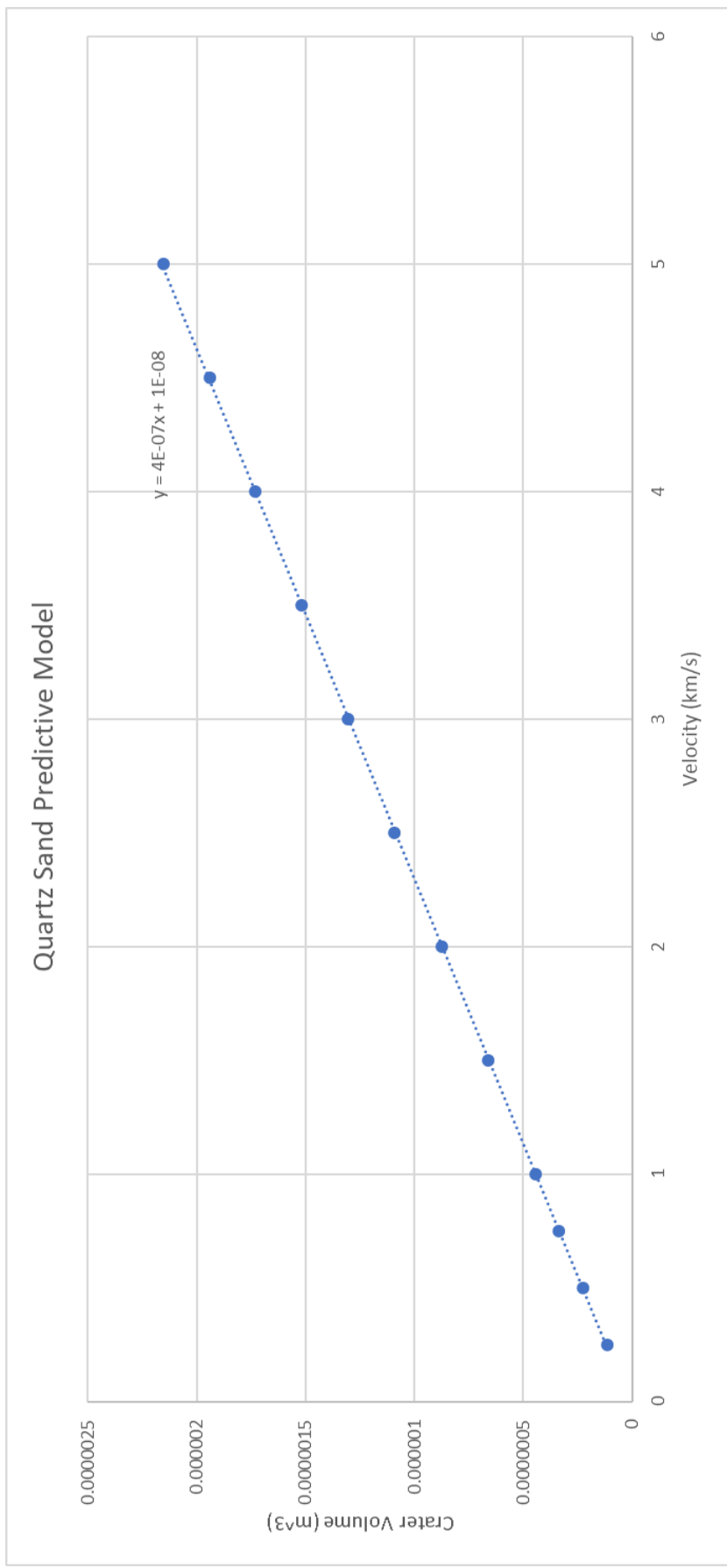


Figure 4.12: Predictive model of crater volume vs projectile velocity (Quartz Sand).

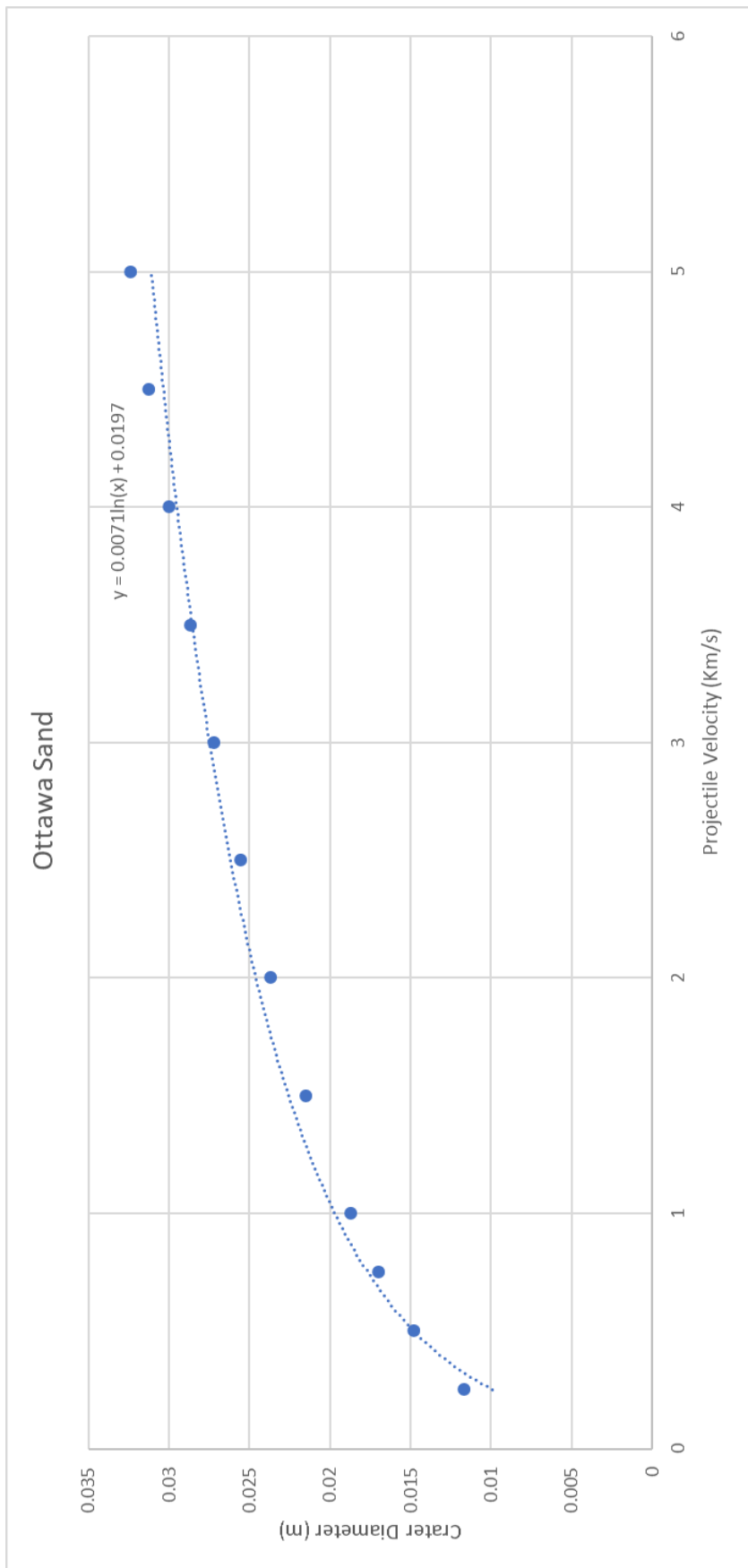


Figure 4.13: Predictive model of the change in crater diameter vs impact velocity (Ottawa sand).

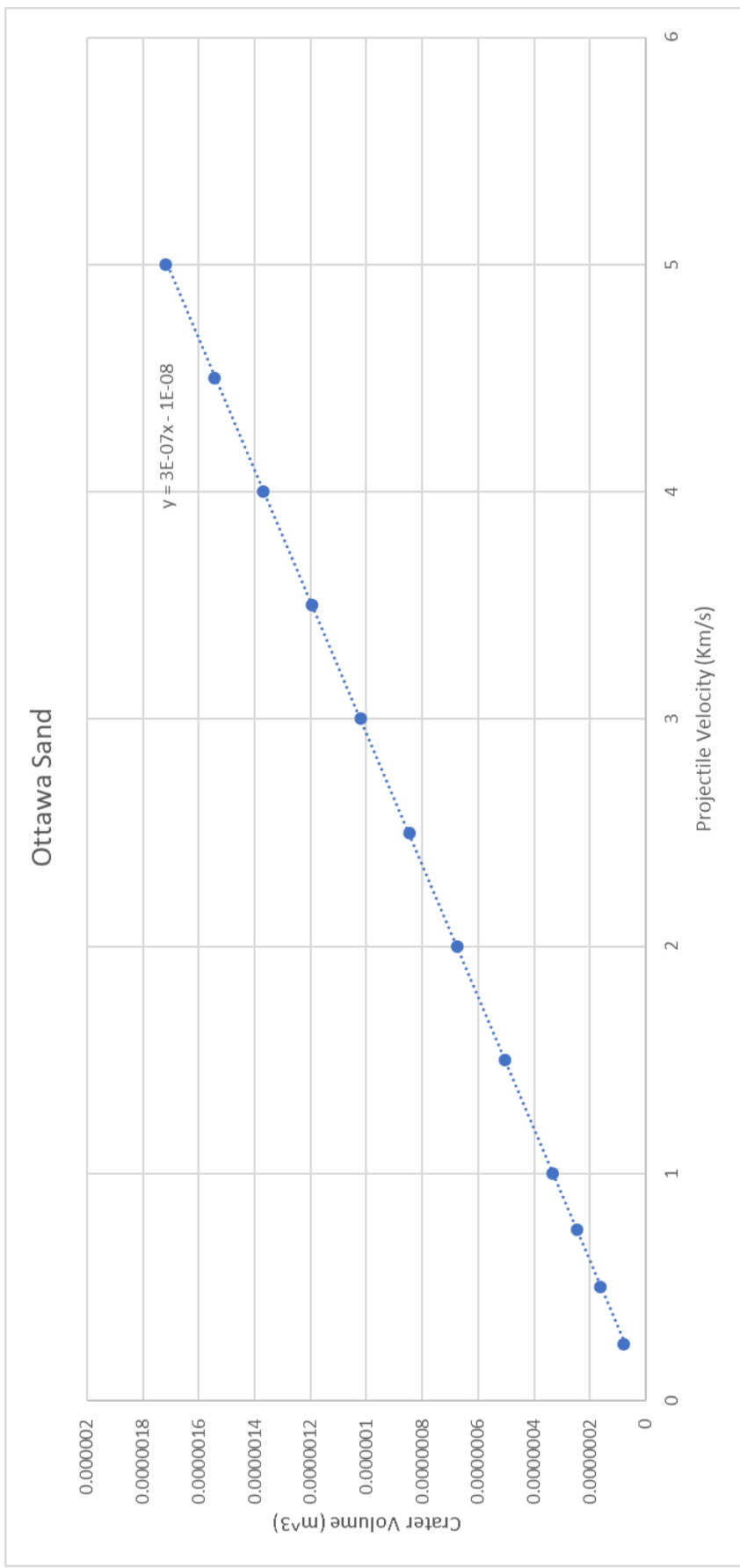


Figure 4.14: Predictive model of the change in crater volume vs impact velocity (Ottawa sand).

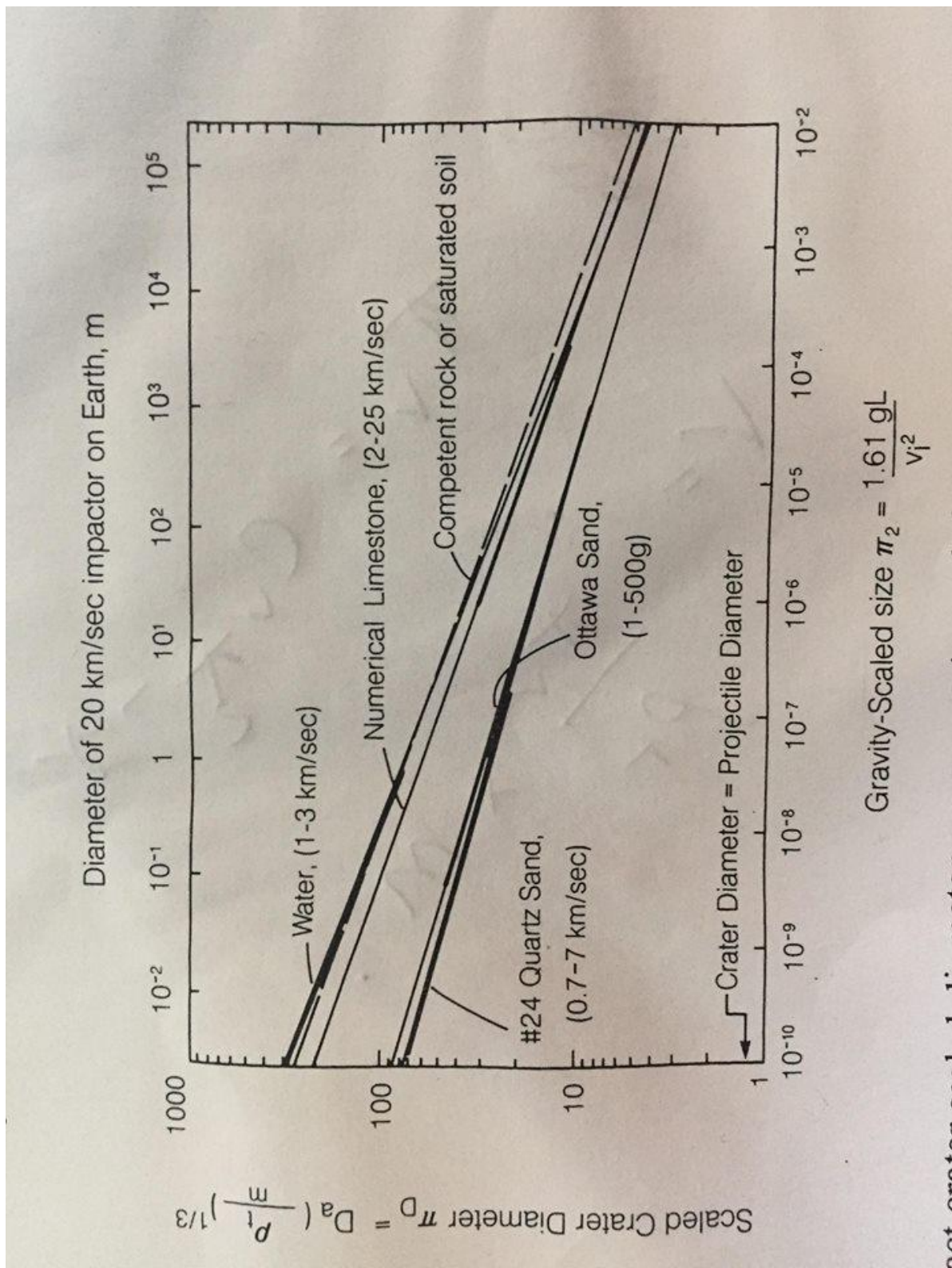


Figure 4.15: Melosh's comparison between the Scaled Crater Diameter and the gravity Scaled Size, his reaches up to 20 km s^{-1} (Figure 7.3, page 118, Melosh, 1989).

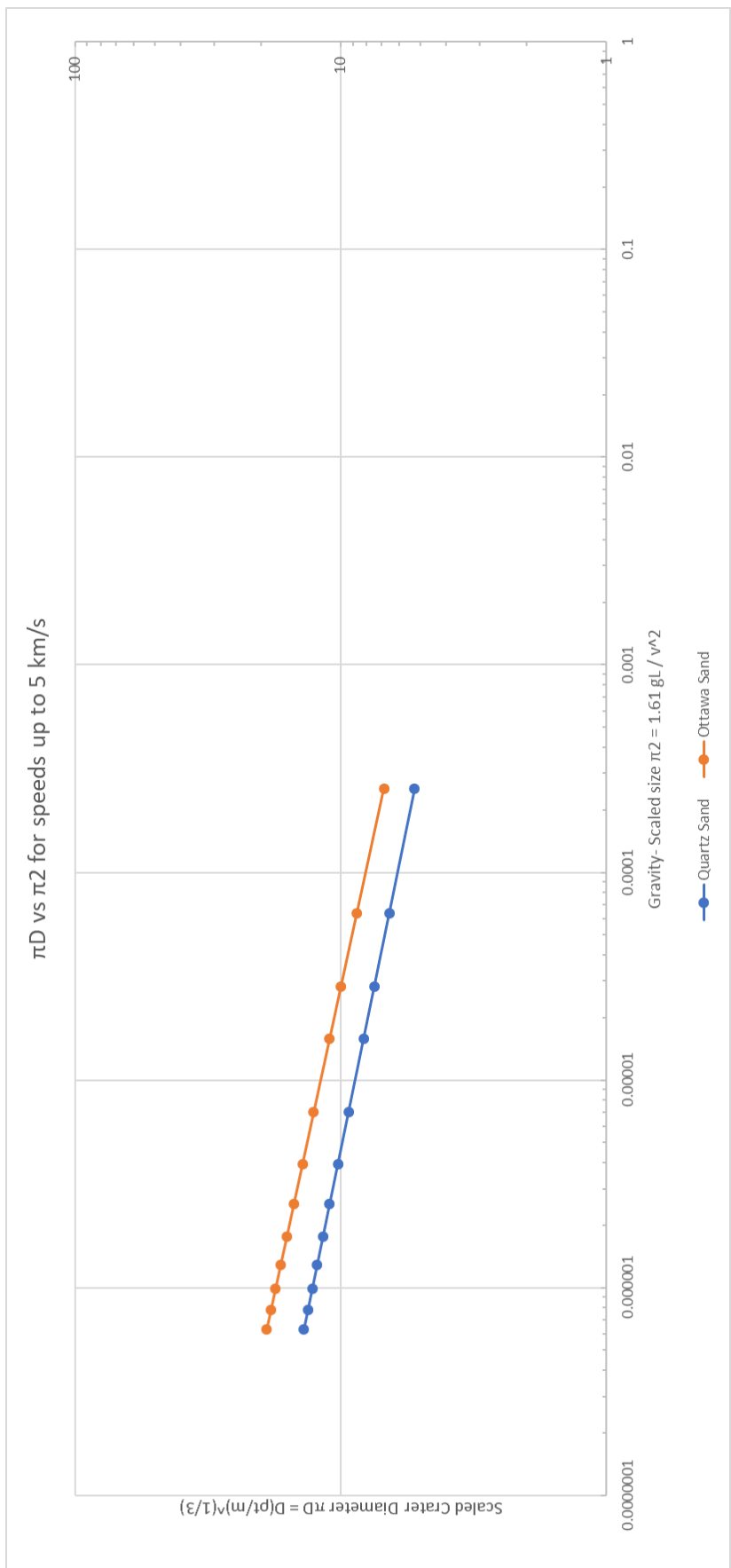


Figure 4.16: Predicative model of π_D vs π_2 Log-graph produced using the data from Table 4.3 reproduced from Impact Cratering (Melosh, 1989).

Crater Number	π_D	π_2	π_V
1.1	19.9726	2.22E-05	5.92E+02
1.2	18.219	2.22E-05	5.92E+02
2.1	26.781	2.04E-05	2.19E+03
2.2	24.551	2.03E-05	2.19E+03
3.1	16.448	1.48E-03	2.98E+02
3.2	15.273	1.48E-04	2.98E+02
4.1	15.273	1.90E-04	1.96E+02
4.2	14.098	1.90E-04	1.96E+02
5.1	23.497	2.49E-05	5.72E+02
5.2	2.5259	2.49E-05	5.72E+02

Table 4.4: Calculated values for π_D , π_2 and π_V from my impact results.

First, I can compare how the diameter and volume of the crater changed with velocity. The results from my experiments can be seen in figure 4.17 and 4.18. Note that I give 2 values for each diameter showing the spread in diameter and volume in my measurements using the crater profile (Table 4.1). It can be seen that similar speeds produced roughly similar crater diameters, even at 0.78 km s^{-1} when 2 different sand types were used. The crater volume vs impact speed is shown in Figure 4.18 and can be seen to grow with speed.

Following this, I compare how my π_2 Gravity-scaled size and π_D scaled crater diameter compare to the predicative models produced previously (Melosh, 1989). These can be seen in Figures 4.19.

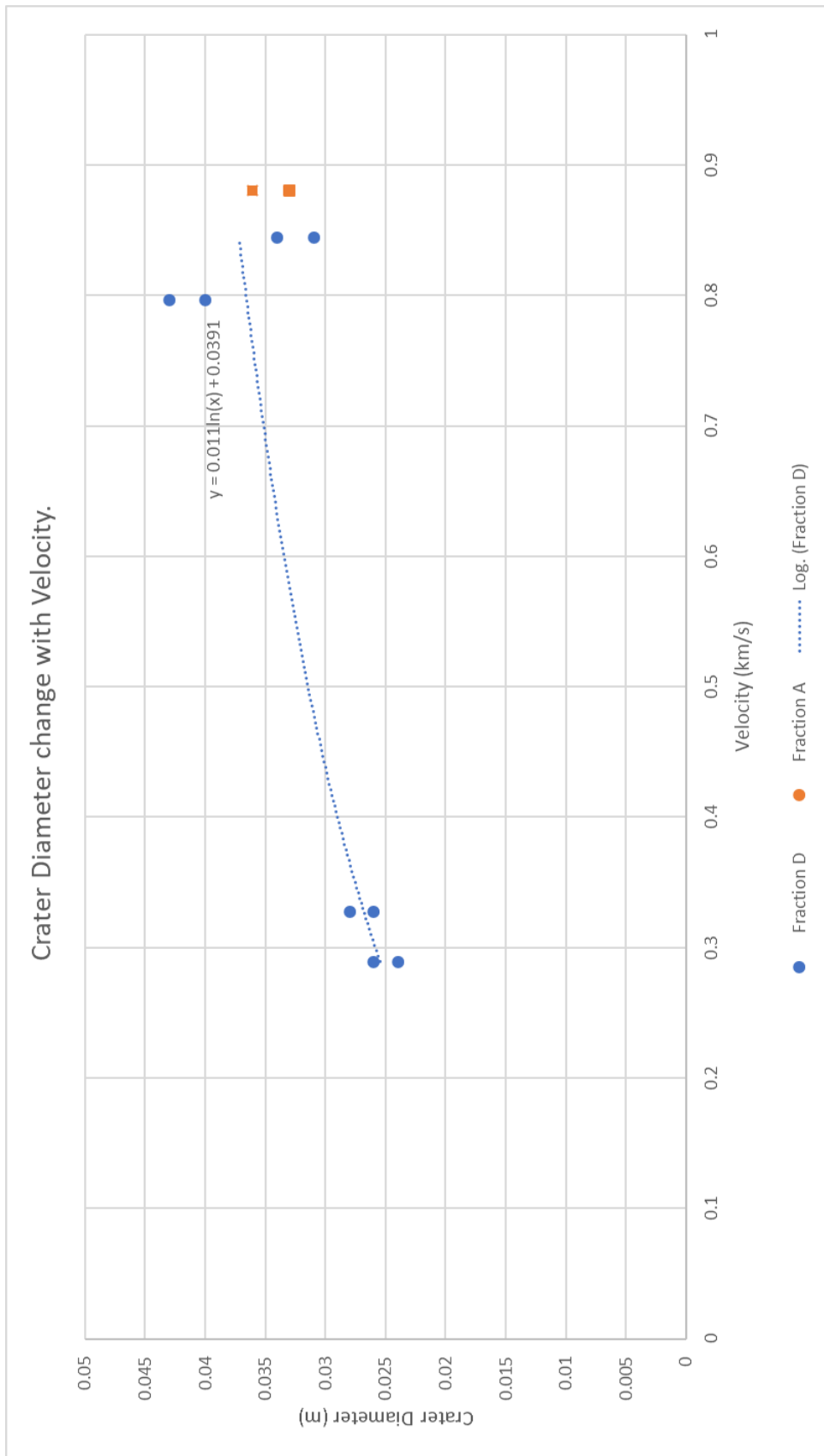


Figure 4.17: From my data, the change in crater diameter with velocity up to around 0.8 km s^{-1} . The blue is the Fraction D sand, and the orange is Fraction A.

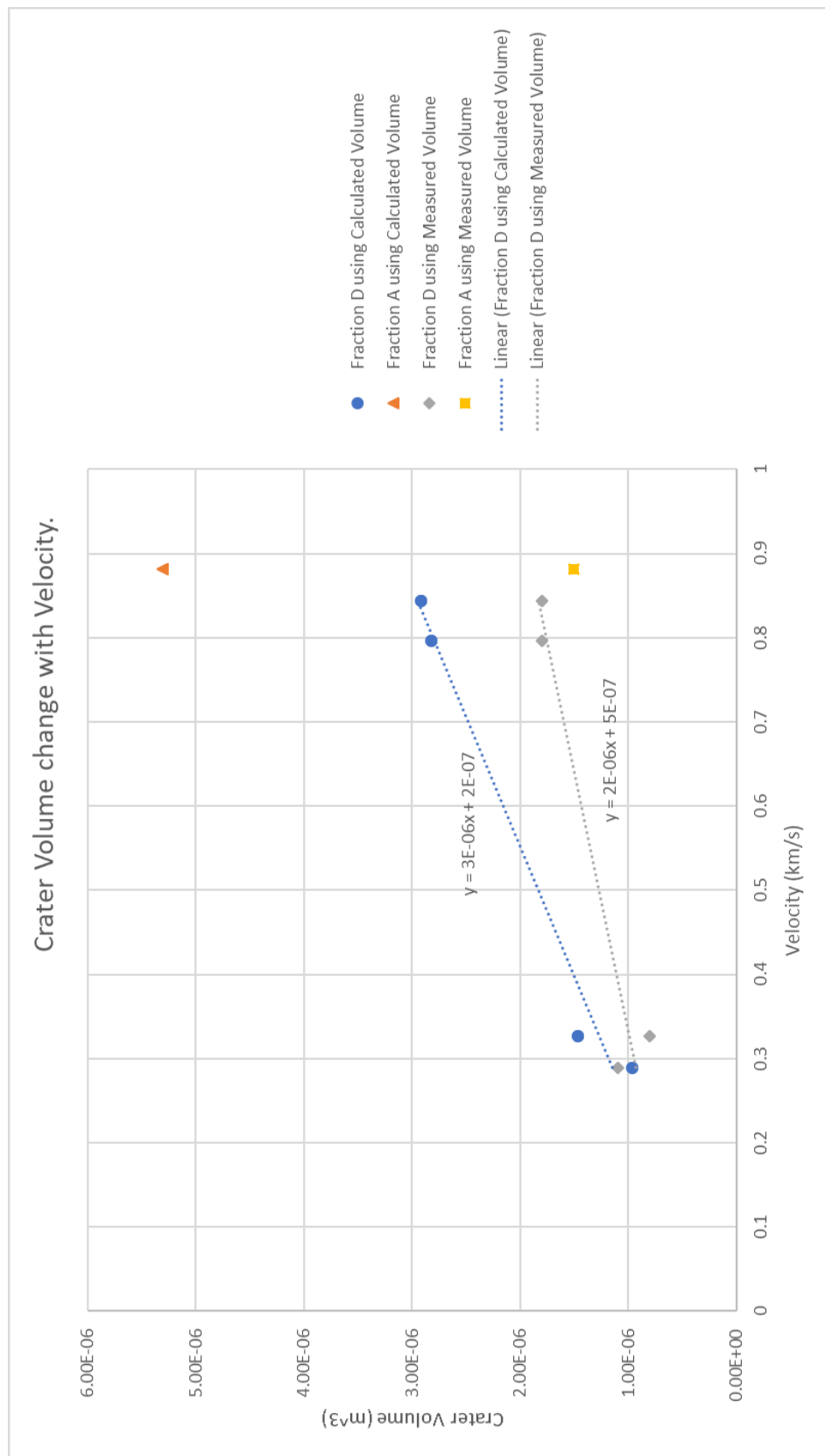


Figure 4.18: From my data, the change in crater volume with velocity, up to around 0.8 km s^{-1} , the blue series is Fraction D sand and the orange is Fraction A. For detail of fit parameters see Table 4.4.

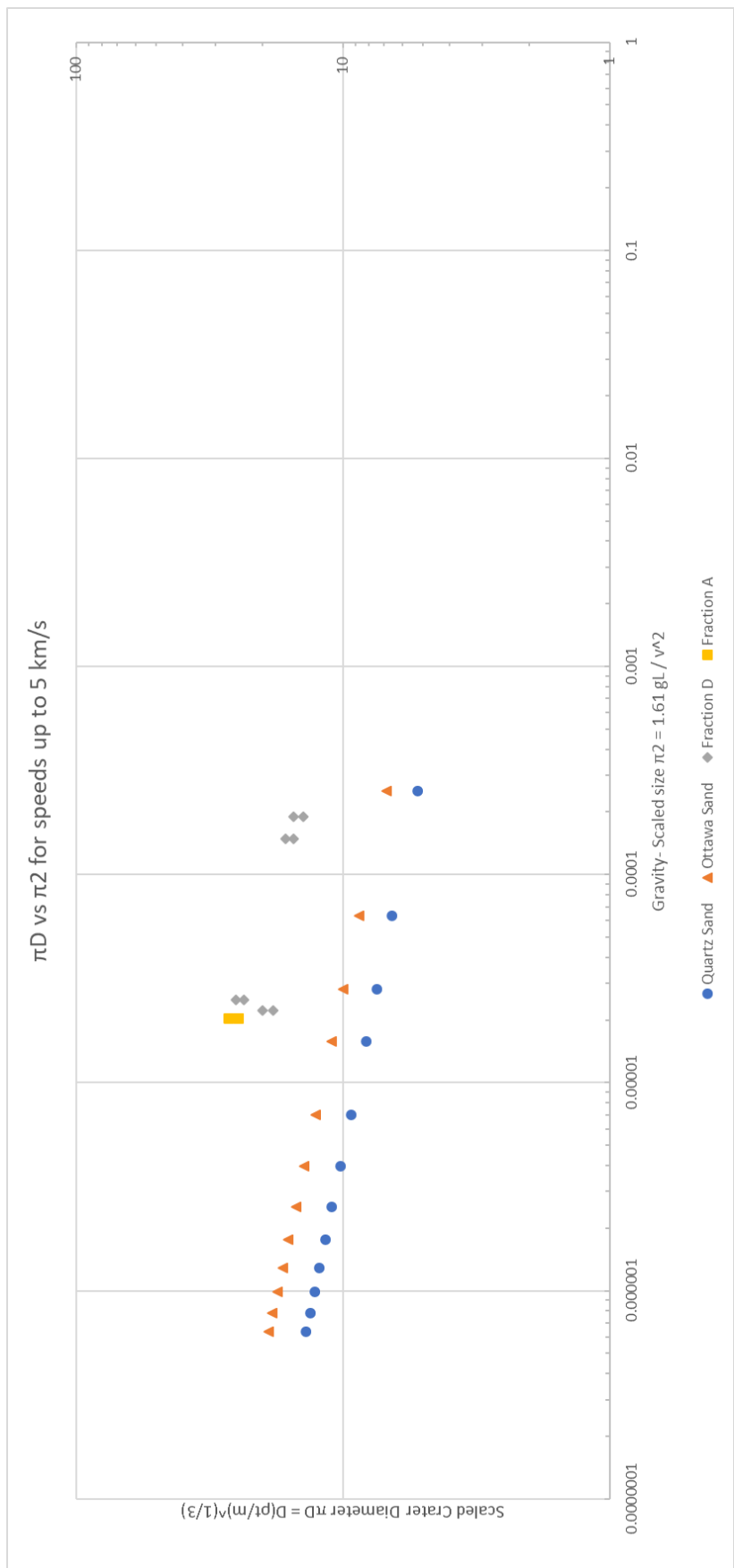


Figure 4.19: My data compared directly to the data previously put together in Impact Cratering (Melosh, 1989)

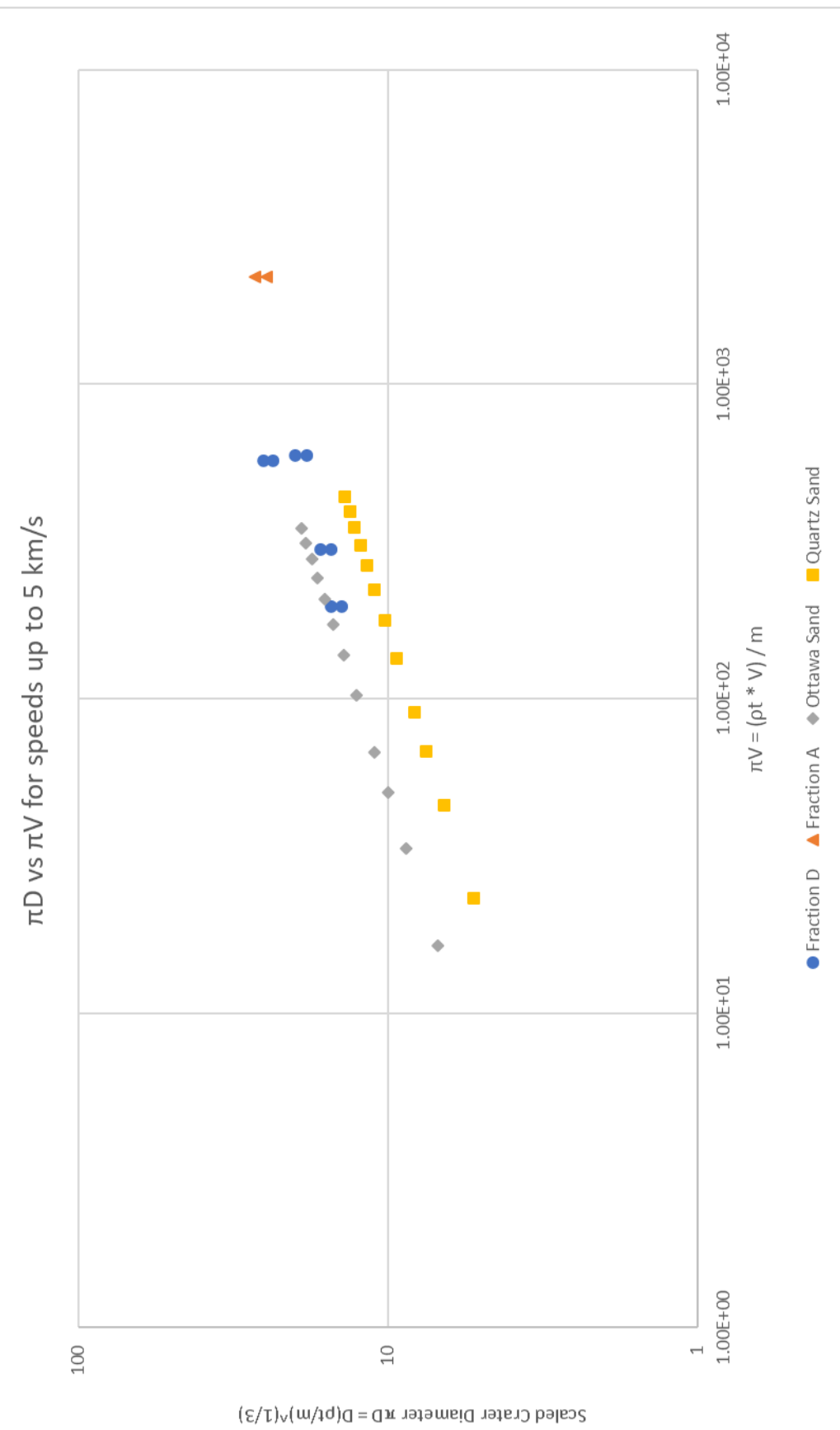


Figure 4.20: My data compared directly to the data previously put together in Impact Cratering (Melosh, 1989)

As the earlier data in Figure 4.19, we can see that the data I collected follows a very similar path to the Ottawa and Quartz sand (Melosh, 1989), albeit with a greater magnitude of π_D at any π_2 by factor that varies slightly with each measurement but is slightly greater than past work by a factor of typically 2. The differences are probably down to the different sand used, however the predictive model seems to fit the pattern very well in that all the data seems to show a similar slope (i.e similar power line). For crater volume, the π_V result of my work fell within these for the different sand used by past work (see Figure 4.20). Table 4.5 brings all the information together into a single place, giving the fits to my data as well as the similar fits to the data based on equations 4.8 and 4.9.

Sand	Diameter vs Velocity	Volume vs Velocity	CD vs π_2	CV vs π_2
Quartz	$y=0.0049\ln(x)+0.0146$	$y=4E-07x+1E-08$	$y=-1.448\ln(x)-7.4178$	$y=2.9549\ln(x)-4.7102$
Ottawa	$y=0.0071\ln(x)+0.0197$	$y=3E-07x-1E-08$	$y=-2.078\ln(x)-11.396$	$y=4.0748\ln(x)-5.5809$
Fraction D	$y=0.011\ln(x)+0.0391$	$y=3E-06x+2E-07$ (Calc.) $y=2E-06x+5E-07$ (Meas.)	$y=-3.22\ln(x)-12.662$	$y=6.7714\ln(x)-21.6256$

Table 4.5: Comparison between the tread lines of the graphs produced in this chapter.

As can be seen from Table 4.4 we can see that my data follows the same pattern as the previous patterns produced in *Impact Cratering* (Melosh, 1989), in that the slope is similar for the diameter, although there is a large difference in volume.

Unfortunately, the development of the new vertical gun is still incomplete. It is hoped to raise the impact speed above 1 km s^{-1} by Christmas 2018, which is after my time in the laboratory. It would be interesting to see how the data would evolve at higher speeds.

4.4 Summary

In this chapter I have given results for comparing how diameter changes with velocities, volume changes with velocity, how π_D changes with π_2 , how π_V changes with π_2 and crater depth profiles for each successful crater produced. I show that whilst there are some changes in magnitude, similar scaling behaviour can be seen for crater diameter in my data and standard data in the literature.

Chapter 5: Conclusion

In conclusion, the prototype vertical light-gas gun at the University of Kent is making steps to reach its full development. The gun is currently (September 2018) at a point where it can fire shots at speeds up to 1 km s^{-1} . Mike Cole is currently working on improving the gun to the point where it can fire projectiles over 1 km s^{-1} , and when this is achieved the gun will be ready for use in experiments on a regular basis. That the gun fires vertically also mean it opens new possibilities for the University, as it allows for vertical shots which means analyses of craters in sand, water and other non-cohesive targets becomes possible.

I have taken data at relatively low-speeds ($< 1 \text{ km s}^{-1}$) and have compared this to the data summarised in the literature *Impact Cratering: A Geological Process* (Melosh, 1989). This has revealed that my data follows the same pattern observed before with work on pi-scaling, with a slight difference, likely due to the different sand type I used combined with my lower impact speed. In the future, someone may be able to come along and complete my data, firing shots at higher speeds, and comparing their data with mine and the earlier work to see if the data continues to follow these trends at speeds greater than 1 km s^{-1} .

By understanding this programme, I can see that the new vertical gun will be very useful in the future for the University's experiments. My five shots were the first successful series of experiments to be carried out with this new gun, and hopefully in the future someone will be able to carry on the data, confirming what I have predicted that the new vertical light-gas gun will follow the same patterns as previous guns, producing consistent results and becoming widely used research tool.

It is believed that target porosity is an important influence on crater size. Once operational it should be possible to explore this in more detail with different sands packed differently. One new area also being developed at the moment is integration of high-speed cameras with the gun. Possible research projects would include cratering in water and observing the craters via the high-speed cameras. In addition, targets can be built in half space containers. That is targets where one side is Perspex (transparent) and the impact occurs close to the side. The crater growth can then be

observed, allowing the flow motion of a sand target to be analysed. Although not done here, sand targets can be sampled after impact and the mean size and shape of the sand grains analysed. This will allow a better understanding of what happens to the sand during impacts. At higher impact speeds achieved this may be particularly useful.

References

- Arslan, K. and Gunes, R. (2018) Experimental damage evaluation of honeycomb sandwich structures with A1/B4C FGM face plates under high velocity impact loads. *Composite Structures*. Vol. 202, pp. 304-312.
- Bridgman, P.W. (1949). The Physics of High Pressure. *G. Bell and Sons, Ltd., London*. Pp.108
- Burchell, M.J. Cole, M.J. McDonnell, A.M. and Zarnecki, J.C. (1999), Hypervelocity Impact Studies Using 2 MV Van De Graaff Accelerator and two-Stage Light-gas gun of the University of Kent at Canterbury. *Measurement Science and technology*, Vol. 10, No. 1.
- Burchell, M. J. Brooke-Thomas, W. Leliwa-Kopystynski, J. and Zarnecki, J. C. (1998) Hypervelocity impact experiments on solid CO₂ targets. *ICARUS*. Vol. 131, Issue. 1, pp. 210-222.
- Burchell, M. J. and Mackay, N. (1998) Numerical modelling of oblique hypervelocity impacts on strong ductile targets. *Meteoritics & Planetary Science*. Vol. 46, Iss. 10, pp. 1510-1524.
- Burchell, M. J. and Whitehorn, L. (2003) Oblique incidence hypervelocity impacts on rocks. *Monthly Notices of Royal Astronomical Society*. Vol. 341, pp. 192-198.
- Corner, J. (1950). Theory of the Interior Ballistics of Guns. *John Wiley and Sons, Inc., New York*, pp.96
- Crozier, W. and Hume, W. (1957). High-Velocity, Light-gas gun. *Journal of Applied Physics*, Vol. 28, No.8, pp.892-894.
- Dhote, K. D. and Verma, P. N. (2018) investigations of hole formation by steel sphere impacting on thin plate at hypervelocity. *Thin-Walled Structures*. Vol. 126 pp. 38-47.
- Fendyke, S. F., Price, M. C., Burchell, M. J. (2013) Hydrocode modelling of hypervelocity impacts on ice. *Advances in Space Research*. Vol. 52, pp. 705-714.

French, B. (1998) Traces of Catastrophe: A Handbook of Shock-Metamorphic Effect in Terrestrial Meteorite Impact Structures. *LPI Contribution* No. 954, Lunar and Planetary Institute, Houston. 120 pp.

Grey, I. D. S. and Burchell, M. J. (2003) Hypervelocity Impact Cratering on Water Ice Targets at temperatures ranging from 100 K to 253 K. *Journal of Geophysical Research*. Vol. 108, No. E3, pp. 6-1 – 6-8.

Hibbert et al. (2017). The Hypervelocity Impact facility at the University of Kent: Recent Upgrades and Specialised Capabilities. *Science Direct: Procedia Engineering*, Vol. 204, pp. 208-214.

Higashide, M. Tanaka, M. Akahoshi, Y. Tohyama, F. (2005) Hypervelocity impact test on metal mesh materials. *Space Debris and Space Traffic management Symposium 2004*, Ed. Bendisch, J. *Science and Technology Series*. Vol. 110 pp. 115-123.

Kearsley, A. T. et al. (2017) Hypervelocity impact in low earth orbit: finding subtle impactor signatures on the Hubble Space Telescope. *14th Hypervelocity Impact Symposium (HVIS 2017)*. *Procedia Engineering*. Vol. 204, pp. 492-499.

Kenkmann, T. (2018) Barringer award lecture. Split-second geology: attempts to understand the structural inventory of impact craters on different scales. *Meteoritics and Planetary Science*. Vol. 53, pp. 6076-6076

Kent, R.H. (1936). Some Special Solutions for the Motion of the Powder Gas. *Physics*, Vol. 7, pp.319

Langweiler, H. (1938). Z. Tech. Physik 19, pp. 416.

Leliwa-Kopystynski, J., Wiodarczyk, I., Burchell, M. J. (2016) Analytical model of impact disruption of satellites and asteroids. *ICARUS*. Vol. 268, pp. 266-280.

Libourel, G. et al. (2018) Hypervelocity Impact Experiments on Metallic Body. *Meteoritics and Planetary Science*. Vol. 53. Pp. 6128-6128

McDermott, K. H., Price, M.C., Cole, M., Burchell, M. J. (2016) Survivability of copper projectiles during hypervelocity impacts in porous ice: A laboratory

investigation of the survivability of projectiles impacting comets or other bodies. *ICARUS*. Vol. 263, pp. 102-117.

McDonnell, J.A.M. (2006). The Open University Planetary Impact Facility: A Compact Two-Stage Light-gas gun for All Impact Angles. *International Journal of Impact Engineering*, Vol. 33, pp. 410-418.

Melosh, H. J. (1989), Impact Cratering: A Geologic Process. *Oxford Monographs on Geology and Geophysics Series* no. 11. ISBN 0 19 504284 0.

Morris, A. J. W and Burchell, M. J. (2017) Laboratory tests of catastrophic disruption of rotating bodies. *ICARUS*. Vol. 296, pp. 91-98.

Schneider, E. and Schäfer, F. (2001). Hypervelocity Impact Research – Acceleration Technology and Applications. *Advanced Space Research*, Vol. 28, No.9, pp.1417-1424.

Morris, A. J. W., Burchell, M. J. (2017) Hypervelocity Impacts in the laboratory on hot rock targets. *14th Hypervelocity impact Symposium (HVIS 2017)*. *Procedia Engineering*. Vol. 204, pp. 300-307.

Schmidt R. M., Housen, K. R. (1987) Some recent advances in the scaling of impact and explosion cratering. *International Journal of Impact Engineering*. Vol. 5, pp. 543-560.

Shrine, N. R. G., Burchell, M. J. and Grey, I. D. S. (2002) velocity scaling of impact craters in Water Ice over the range 1 to 7.3 km s⁻¹. *ICARUS*. Vol. 155, pp. 475-485.

Stilp, A.J. (1987). Review of Modern Hypervelocity Impact Facilities. *International Journal of Impact Engineering*. Vol. 5, pp.613-621.

Verma, P. N. and Dhote, K. D. (2018) Characterising primary fragment in debris cloud formed by hypervelocity impact of spherical stainless-steel projectile on thin steel plate. *International Journal of Impact Engineering*. Vol. 120, pp. 118-125.

<http://hyperphysics.phy-astr.gsu.edu/hbase/Solar/soldata3.html>

<https://ai2-s2-public.s3.amazonaws.com/figures/2017-08-08/443b08b1f64c775bc063fbecbf1ca665757c2cbc/2-Figure1.1-1.png>

<https://www.barringercrater.com/the-crater/#history-banner>